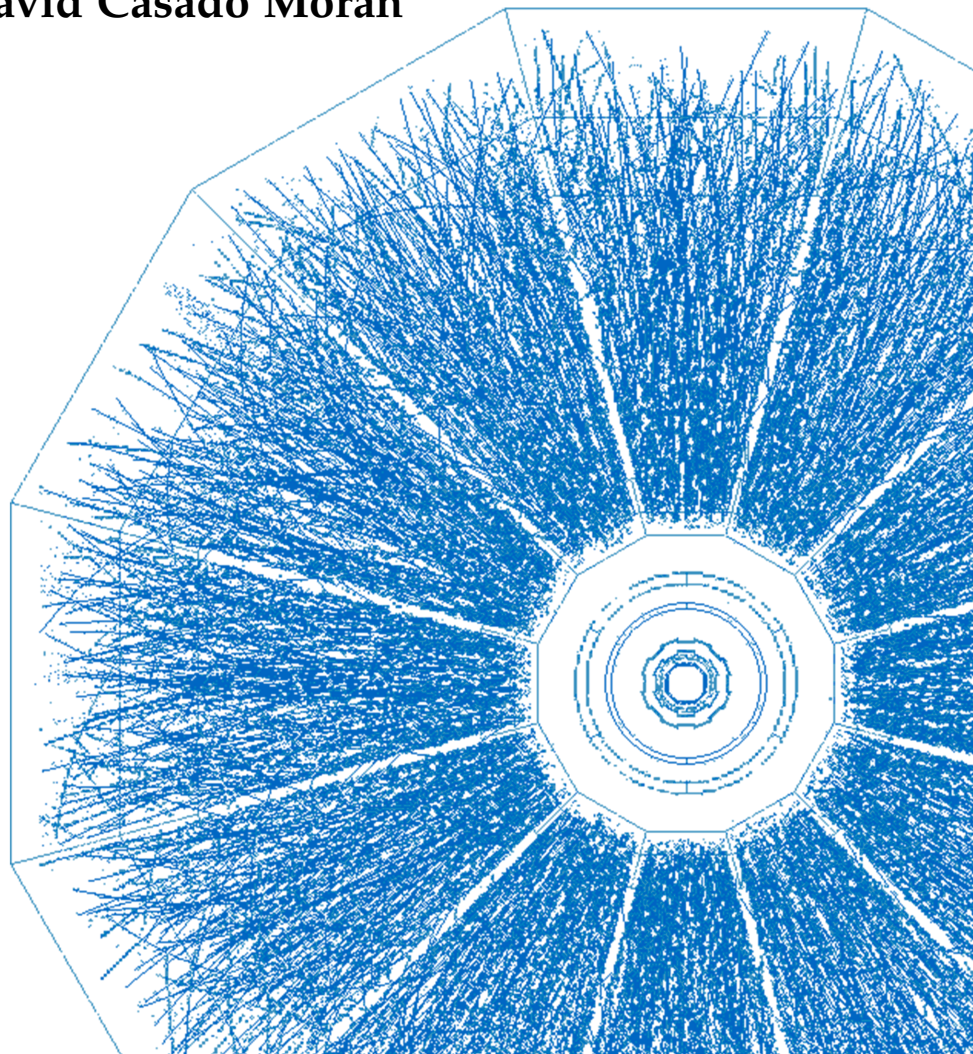


Master's Thesis

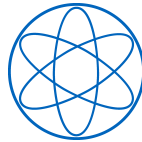
Comparison of the STAR Au–Au antideuteron measurement with a Wigner function based coalescence model

David Casado Morán





TECHNISCHE UNIVERSITÄT MÜNCHEN



Fakultät für Physik

Comparison of the STAR Au–Au antideuteron measurement with a Wigner function based coalescence model

Vergleich der STAR Au–Au-Antideuteron-Messung mit einem auf der Wigner-Funktion basierenden Koaleszenzmodell

Master's Thesis

Author: David Casado Morán
Examiner: Prof. Dr. Laura Fabbietti
Supervisor: Maximilian Horst
Date: 16.10.2023

I confirm that the results presented in this master's thesis is my own work and I have documented all sources and materials used.

Ich versichere, dass ich diese Masterarbeit selbstständig verfasst und nur die angegebenen Quellen und Hilfsmittel verwendet habe.

Munich, 16.10.2023

David Casado Morán

Abstract

Coalescence is a major model used to describe the formation of light (anti)nuclei in high-energy collisions. It is based on the assumption that two nucleons close in phase space can coalesce and form a nucleus. Antideuteron and antihelium nuclei have been proposed as a detection channel for dark matter annihilations and decays in the Milky Way, due to the low astrophysical background expected. In order to correctly interpret any future antinuclei measurement in space, the production of antinuclei has to be well understood. In this Master's Thesis, a more advanced approach is employed combining event-by-event Monte Carlo simulations with a microscopic coalescence picture based on the Wigner function formalism. The antiproton production in the event generator EPOS 3 and the transport model SMASH is compared to measurements from the STAR Collaboration.

Contents

1. Introduction	1
2. Light Nuclei production	4
2.1. Space-time evolution of the heavy-ion collision	4
2.2. Nuclear matter production	6
2.2.1. Statistical Hadronisation Model	6
2.2.2. Coalescence Model	7
2.3. Impact parameter, rapidity and charged particle multiplicity	11
3. EPOS3 Event Generator	13
3.1. Working principle	13
3.2. Accessing EPOS	14
4. SMASH transport model	18
4.1. Model description	18
4.1.1. Collision Criterion	18
4.1.2. Propagation	19
4.1.3. Test particles	20
4.1.4. Mean-field Potential	20
4.1.5. Nearest Neighbor Method	20
4.2. SMASH Initialization	21
4.2.1. Nuclear Collisions	21
4.2.2. Infinite matter	23
4.2.3. Expanding sphere	23
4.2.4. Afterburner	23
5. Beam Energy Scan Program	24
5.1. QCD Phase diagram	24
5.2. STAR Experiment	25
6. Correcting the Event Generator	28
6.1. Correction Scheme	28
6.2. Charged Particle Multiplicity	29
6.3. Source Size	30
6.4. Momentum Distributions	34
7. (Anti-)deuteron production spectra	40
8. Summary and Outlook	46

Contents

A. Appendix - SMASH Afterburner	47
A.1. Configuration file	47
A.2. Input List of Particles	47
List of Figures	50
List of Tables	53
Bibliography	54

1. Introduction

In our galaxy, light antinuclei composed of antiprotons (\bar{p}) and antineutrons (\bar{n}) can be produced through high-energy cosmic-ray collisions with the interstellar medium or could also originate from the annihilation of dark-matter particles that have not yet been discovered [1]. On Earth, there are no natural forms of antinuclei, such as antideuterons \bar{d} ($\bar{p}\bar{n}$), antihelium-3 ${}^3\bar{\text{He}}$ ($\bar{p}\bar{p}\bar{n}$), and antihelium-4 ${}^4\bar{\text{He}}$ ($\bar{p}\bar{p}\bar{n}\bar{n}$). The only way to produce and study antinuclei with high precision is to create them at high-energy particle accelerators such as the LHC or RHIC.

In nuclear physics, the production mechanism of these antinuclei and their interaction helps to understand the strong interaction binding nucleons into nuclei [2]. From an astrophysical view, antinuclei can travel large distances through our galaxy without being absorbed and are annihilated with regular matter. Antinuclei can be produced naturally in space, like in collisions between cosmic rays and the interstellar medium, with really small expected production rates. Another scenario is that light antinuclei are produced by the annihilation of dark-matter particles, like weakly interacting massive particles [3] and exotic sources like antistars [4]. Identifying natural sources of antinuclei can give us insights into evidence of the existence of dark-matter particles. Knowledge of antinuclei's production and annihilation probabilities is crucial [1].

Fritz Zwicky first introduced Dark Matter [5] in 1933 as a possible explanation for the high-velocity dispersion observed inside the Coma Cluster. Following this discovery, Rogstad and Shostak [6] in 1972 introduced the first rotation curves of galaxies, making it evident that some invisible matter must be present. Bosma [7] and Rubin et al. [8] further confirmed this hypothesis. At this time, dark matter was seen as all possible non-luminous matter, including neutron and dwarf stars. Presently, dark matter is usually defined as nonbaryonic, elementary particles [9]. It constitutes 27 % of the total energy in our Universe, constrained by studying predictions from the cosmic microwave background [10], rotational curves of galaxies [11] and gravitational lensing of galaxy clusters [12].

The different methods to detect dark matter particles vary from direct and indirect ways to experiments in high-energy particle accelerators that can be indirect or direct experiments. In direct detection methods, the dark matter candidate is measured directly either by measuring photons in the lab or the recoil of a standard model particle, often trying to interact with galactic dark matter [13]. Indirect detection channels include measuring the decay products of dark matter candidates in our Universe, where one dark matter candidate and one antiparticle (Dirac) or two dark matter candidates (Majorana) will annihilate. These decay products will be part of high-energy cosmic rays detected on Earth.

Another production channel for dark matter candidates is the secondary production within these high-energy cosmic rays when interacting with the interstellar medium,

1. Introduction

producing antinuclei. A further tertiary contribution from the rescattering of these produced antinuclei is also present. This last contribution is studied to constrain the background and to better disentangle the Dark Matter signal from the Standard Model background.

A graphical representation of the production channels of antideuterons in our Universe is presented in Fig. 1.1. The primary detection channel of antideuterons consists of dark matter annihilation into a W^+W^- pair, further decaying into hadrons. The secondary production is also depicted, where an antideuteron is formed from a collision between high-energy cosmic rays and atoms from the interstellar medium. Finally, a tertiary contribution is shown where an antideuteron with lower momentum than secondary antineutrons is formed from the rescattering of the secondary production.

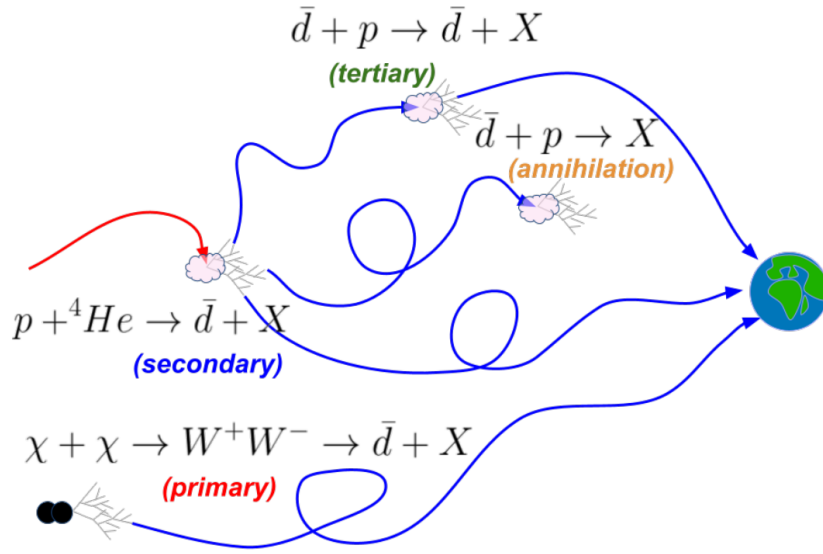


Figure 1.1.: Graphical representation of the antideuteron production channels present in our Universe and measured on Earth. Primary contributions are carried by two matter particles annihilating into a W^+W^- pair, decaying into an antideuteron and other products. Secondary production occurs when high-energy cosmic rays collide with atoms from the interstellar medium. Tertiary channels include antideuterons that scatter off the interstellar medium, elastically losing momentum compared to secondary antideuterons.

These different channels for antideuteron production form the antideuteron flux measured on Earth. The signal-to-background ratio is theorized to be three or four orders of magnitude lower for the low kinetic regime, thus making antideuterons an important particle for indirect searches of dark matter candidates.

In this work, the production of light nuclei is introduced in Chapter 2, giving some insight into the different models for nuclear matter production. In Chapter 3, the EPOS3 event generator is presented. Chapter 4 describes the SMASH transport model used similarly to EPOS to simulate heavy-ion collisions. Chapter 5 presents a description of the BES program and the STAR experiment. In Chapter 6, the tuning of the event

1. *Introduction*

generators is explained to get a prediction of nuclear production free of biases from the event generator. Finally, Chapter 7 presents the results of antideuteron spectra obtained from EPOS and SMASH for a Au–Au collision at two different energies.

2. Light Nuclei production

A fundamental distinction between elementary particle collisions and heavy-ion collisions (HIC) is made in particle physics. The critical disparity lies in the behavior of the particles generated during the primary collisions between the incoming nucleons [14].

Unlike elementary particle collisions, where the resulting particles can escape into the surrounding vacuum, the ones produced in HIC cannot immediately disperse but a dense and strongly interacting form of matter is formed. When this matter thermalizes rapidly enough and achieves a sufficiently high energy density, it becomes a state known as quark-gluon plasma (QGP). Further, the resulting particles rescatter with each other. Understanding the behavior and characteristics of this system is one of the central objectives of studying the matter created in the very early universe. The space-time evolution of a HIC is illustrated in Fig. 2.1; if the energy of the collision is high enough, a QGP is formed while a low-energy collision presents its absence [15, 16].

2.1. Space-time evolution of the heavy-ion collision

During the initial moments of the collision, the system enters a pre-equilibrium stage. During this stage, hard processes play a dominant role. These processes involve a large momentum transfer between the scattering partons, producing particles with large transverse momenta or masses. These particles undergo elastic and inelastic scattering.

Consequently, in high-energy collisions, the partons interact several times, losing energy. Due to these hard scatterings, the system can be seen as a hot interacting medium redistributing energy among the other particles until it reaches thermal equilibrium, where all the participating particles get an equal energy distribution, making the medium thermalized. If the energy density of the collision surpasses a certain threshold $\sim 1\text{GeV}/\text{fm}^3$, it forms a QGP. The QGP can experience thermal pressure gradients due to anisotropies in the initial collision. At the same time, the system undergoes a phase of expansion, which is well described by relativistic hydrodynamics. As a result, the system gradually cools down, leading to a decrease in its energy density. Once the energy density of the system reaches a critical value, approximately $\epsilon_c \simeq 1\text{GeV}/\text{fm}^3$, the partons within the system further hadronize into a Hadron Resonance Gas (HRG). This HRG continues to expand and cool down. On the other hand, for small colliding systems, if the energy density of the collision is not sufficiently high, the QGP phase is left out, and the free partons directly combine to form an HRG.

Eventually, a point is reached where the transferred momentum between the hadrons falls below the threshold for inelastic interactions, known as the chemical freeze-out,

2. Light Nuclei production

characterized by the critical temperature t_{chem} . At this stage, the abundance of particle species becomes fixed, except for weakly decaying particles and resonances.

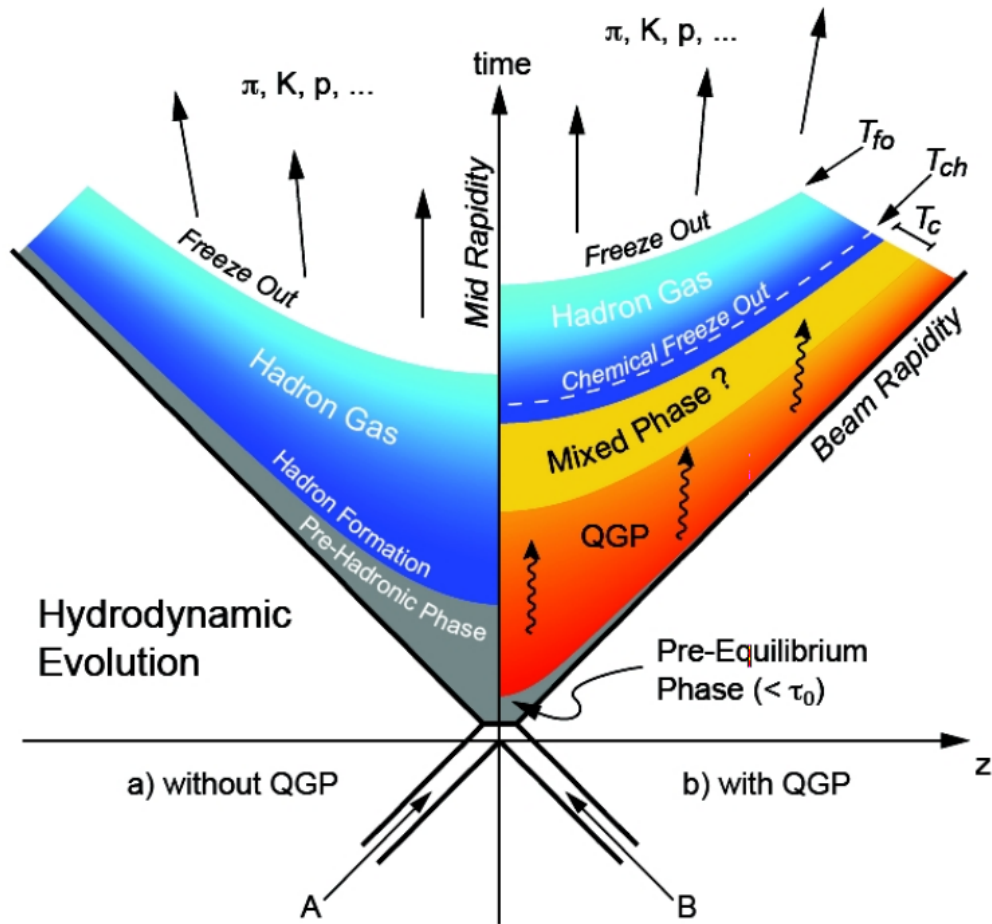


Figure 2.1.: Space-time diagram illustrating the evolution of a central heavy ion collision. The z -axis represents the direction parallel to the beam line. The diagram highlights two scenarios: on the right, the presence of a QGP, while on the left, the absence of it. Taken from [16]

Following the chemical freeze-out, the resulting hadrons undergo rescattering; these can scatter among themselves while moving outwards before the system has expanded enough that the hadrons get free. While the system expands, the matter becomes increasingly dilute, reaching a point where the mean free path of the hadrons surpasses the system size, and even elastic scattering ceases. At this stage, known as kinetic freeze-out, the kinematic distribution of particles in the final state is fixed.

2.2. Nuclear matter production

The mechanism behind light (anti-)nuclei production remains poorly understood. Phenomenological models for producing these light (anti-)nuclei rely on Statistical Hadronisation Models (SHMs) and coalescence models. These models offer different perspectives and approaches to provide insights into the underlying processes of producing light (anti-)nuclei.

2.2.1. Statistical Hadronisation Model

The Statistical Hadronization Model (SHM) adequately describes the formation of hadrons in high-energy collisions. It is a valuable tool for predicting the yields of hadron species produced during particle collisions [16, 17]. The concept of using statistical principles applied to multi-particle production in high-energy collisions was first introduced by Enrico Fermi in 1950 [18]. In his study, Fermi proposed the hypothesis that particles originate from an excited region that evenly populates all accessible phase space states, i.e. thermodynamic equilibrium [19], and does not rely on a microscopic production mechanism.

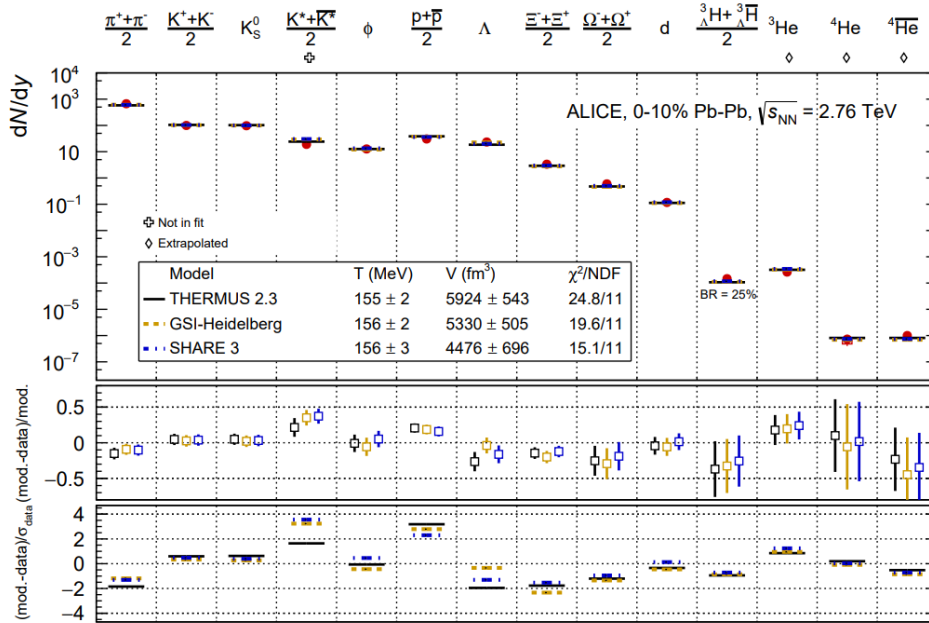


Figure 2.2.: Three different statistical hadronization model fits the selected mesons, hadrons, and light (anti-)nuclei yields in Pb-Pb collisions at $\sqrt{s_{NN}}=2.76$ TeV. Taken from [20].

In the SHM, also called the Thermal Model, the particle yields depend on two free parameters: the temperature T_{chem} of the system at chemical freeze-out and the baryon chemical potential μ_B , degree of matter-antimatter asymmetry present in the system. It is expected that for measurements at large energies and mid-rapidity, explained in Sec. 2.3, the baryon chemical potential goes to 0.

2. Light Nuclei production

In principle, light nuclei in HIC might seem unexpected because $T_{chem} \approx 100$ MeV is typically much higher than the binding energy of these nuclei of the order of 1 MeV per nucleon [21]; this is due such loosely bound objects have much larger sizes than the inter-particle separation at the time of chemical freeze-out [22]. However, it is essential to note that the thermal model does not consider the internal structure of the nuclei. Instead, it predicts their yields without any dynamical description of their formation.

Fig. 2.2 shows the thermal model's predictions for the production yields of (anti-)nuclei and hypernuclei i.e. nuclei where a neutron is replaced with a hyperon [23], for Pb–Pb collisions at 2.76 TeV, compared to ALICE measurement. At lower energies, the production of nuclei is favored over the production of antinuclei; solid and dashed lines represent the three different models. This behavior arises from the relationship between the collision energy and μ_B . At lower collision energies, where μ_B deviates from zero, matter production is preferred over antimatter. As the collision energy increases, μ_B approaches zero, resulting in equal predictions for producing matter and antimatter.

For further information on the SHMs, see Ref. [16].

2.2.2. Coalescence Model

The coalescence model, initially proposed by Butler and Pearson [24] in 1963, was developed to study proton-nucleus collisions, forming high-energy deuterons. It states that (anti-)nucleons ((anti-)protons and (anti-)neutrons) close in phase space will coalesce and form an (anti-)nucleus.

One key observable of the coalescence model is the coalescence parameter B_A , which gives the probability that nucleons will coalesce and form (anti-)nuclei, expressed as

$$B_A = E_A \frac{d^3 N_A}{dP_A^3} \bigg/ \left(E_p \frac{d^3 N_p}{dP_p^3} \right)^Z \left(E_n \frac{d^3 N_n}{dP_n^3} \right)^N \quad | P_p = P_n = P_A/A, \quad (2.1)$$

where $E_A \frac{d^3 N_A}{dP_A^3}$ is the invariant yield of nuclei with mass number A formed out of Z protons and N neutrons, $E_p \frac{d^3 N_p}{dP_p^3}$ the invariant yield of protons and $E_n \frac{d^3 N_n}{dP_n^3}$ the invariant yield of neutrons[25].

Spherical Approximation

The spherical approximation is one of the more straightforward implementations of the coalescence model [26]. In this model, a proton and a neutron coalesce if they are within a sphere of radius p_0 in momentum space or one of them is in a sphere around the other nucleon, as shown in Fig. 2.3.

In this approximation, only momentum-space is considered, and the radius p_0 is a free parameter dependent on the reaction type and the center-of-mass energy \sqrt{s} . This works particularly well for systems like e^-e^+ and pp collisions, where the system size ($\sigma_{(pp)} \approx \sqrt{2}\sigma_{(e^\pm)}$ with $\sigma_{(e^\pm)} \approx 1$ fm [25]) is similar to the nucleus size of the deuteron ($r_d \approx 2.12$ fm [27]). On the other hand, larger systems (e.g., Au–Au/Pb–Pb collisions) have a bigger size than the nucleus size; even if their momenta are comparable, nucleons could not coalesce into a nucleus due to their spatial separation.

2. Light Nuclei production

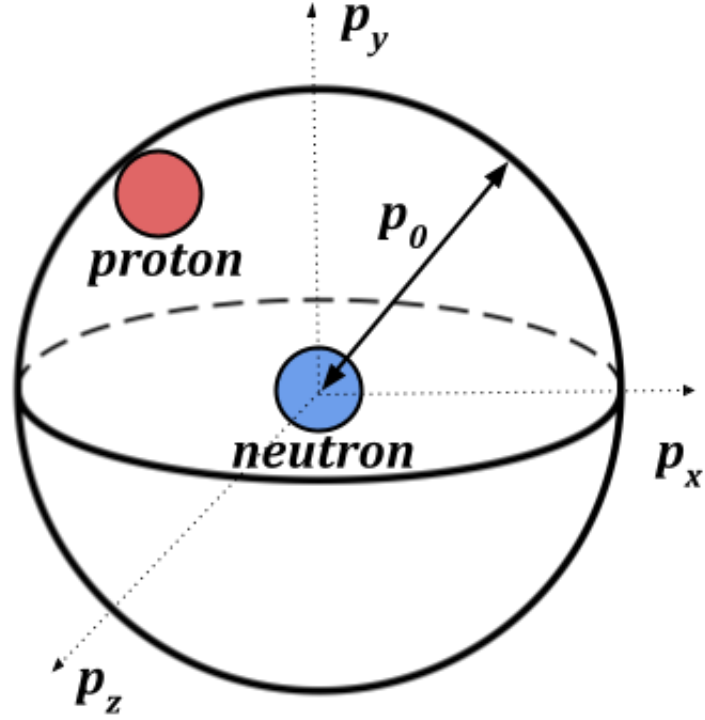


Figure 2.3.: Graphical representation of a proton-neutron pair, where a proton is within a sphere of radius p_0 in momentum-space around a neutron.

If we consider equal proton and neutron yields, i.e., assuming isospin symmetry, the coalescence parameter B_A in this spherical approximation can be expressed as:

$$B_A = A \left(\frac{4\pi}{3} p_0^3 \right)^{A-1} \frac{m_A}{m_p^A} \quad (2.2)$$

Where A is the mass number of the nucleus, m_A the mass of the nucleus, m_p the proton mass, and p_0 the maximum radius in momentum-space allowed for coalescence to take place.

This approach can be improved by considering the momentum correlations between nucleons, which can be incorporated through Monte Carlo (MC) simulations or analytical approaches, often on an event-by-event basis. The analytical approach consists of assuming uncorrelated proton and neutron momentum distributions, factorized as

$$\frac{dN_{p,n}}{dk_p^3 dk_n^3} = \frac{dN_p}{dk_p^3} \frac{dN_n}{dk_n^3}. \quad (2.3)$$

This approximation fails to estimate the true deuteron yields at low energies since, for example, at energies close to the antideuteron production regime ($\sqrt{s} \approx 6m_p$ where six nucleons are present to form an antideuteron), the production of antiparticles is suppressed when compared to an uncorrelated production [28]. A further simplification can be made if we equate the proton and neutron yields, obtaining an invariant deuteron

2. Light Nuclei production

yield,

$$E_d \frac{dN_d}{d\vec{k}_d^3} = B_2 \left(E_p \frac{dN_p}{d\vec{k}_p^3} \right). \quad (2.4)$$

In the Monte Carlo approach, the simulations can explain the yields and the correlations of the production of nuclei and are taken directly from event generators. However, event generators (e.g., EPOS3, PYTHIA) do not reproduce nature correctly, so one needs to correct the event generator to reproduce the desired data, which will be described in Chapter. 6.

Advanced Coalescence Model - Wigner Function Formalism

The Advanced Coalescence Model is based on the Wigner function of the deuteron; it was first introduced by Scheibl and Heinz [29] in 1999. This model gives a semi-classical picture of the formation region's size and the momentum correlations between the constituent nucleons. The Wigner function [30] of an object is expressed as

$$D(r, q) = \frac{1}{\pi\hbar} \int_{-\infty}^{\infty} \psi^*(q+p)\psi(q-p)e^{2irp/\hbar} dq, \quad (2.5)$$

where $\psi(q)$ is the wave function of the deuteron, and the Wigner function is a probability distribution in phase space for a deuteron to exist with a relative momentum and a distance between its constituents. Following closely the derivations from [25] for the case of deuteron production, one can start from a system formed with a proton and a neutron in a frame of reference where their Center of Mass (CoM) is non-relativistic.

One can express the number of deuterons with momentum \mathbf{P}_d with the projection of the deuteron density matrix ρ_d onto the two-nucleon density matrix ρ_{nucl} as

$$\frac{d^3N_d}{dP_d^3} = \text{tr} \{ \rho_d \rho_{nucl} \}. \quad (2.6)$$

In this approach, the deuteron density matrix is a pure state, $\rho_d = |\psi_d\rangle \langle \psi_d|$. For the two-nucleon (described out of a proton and a neutron) density matrix, the spin and isospin can be taken into account by introducing a statistical factor $S = 3/8$, so one can express it as $\rho_{np} = |\psi_p\psi_n\rangle \langle \psi_n\psi_p|$. The average multiplicities of protons N_p and neutrons N_n per event can be obtained with the normalization $\langle \psi_n\psi_p | \psi_p\psi_n \rangle = N_p N_n$.

Using a coordinate description $|x_1x_2\rangle$ for the positions of the two nucleons, the evaluation of the trace from Eq. 2.6 is obtained

$$\frac{d^3N_d}{dP_d^3} = S \int d^3x_1 d^3x_2 d^3x'_1 d^3x'_2 \psi_d^*(x_1, x_2) \psi_d(x'_1, x'_2) \langle \psi_n^\dagger(x'_2) \psi_p^\dagger(x'_1) \psi_p(x_1) \psi_n(x_2) \rangle \quad (2.7)$$

where ψ_d is the deuteron wave function, ψ_p the proton wave function and ψ_n the neutron wave function in the coordinate system. Using the Wigner function formalism, we replace the two-nucleon density matrix with its two-body Wigner function [29],

2. Light Nuclei production

$$\begin{aligned} \langle \psi_n^\dagger(x'_2) \psi_p^\dagger(x'_1) \psi_p(x_1) \psi_n(x_2) \rangle &= \int \frac{d^3 p_n}{(2\pi)^3} \frac{d^3 p_p}{(2\pi)^3} W_{np} \left(p_n, p_p, \frac{x_2 + x'_2}{2}, \frac{x_1 + x'_1}{2} \right) \\ &\times \exp [i p_n \cdot (x_2 - x'_2)] \exp [i p_p \cdot (x_1 - x'_1)]. \end{aligned} \quad (2.8)$$

For further simplification, the coordinate transformations are computed as $r_p = (x_1 + x'_1)/2$ for the position of the proton, $r_n = (x_2 + x'_2)/2$ for the position of the neutron, their separation $r = r_n - r_p$, $\xi = x_1 - x'_1 - x_2 + x'_2$ and $\rho = (x_1 - x'_1 + x_2 - x'_2)/2$. For the momentum, $p = p_n + p_p$ and $q = (p_n - p_p)/2$.

Looking at the two-nucleon Wigner function W_{np} , one can proceed by assuming no correlation between momentum and coordinate space, namely $W_{np}(r_n, r_p, p_n, p_p) = G_{np}(p_n, p_p) \times H_{np}(r_n, r_p)$. Further, assuming no correlation between the spatial distribution of protons and neutrons $H_{np}(r_n, r_p) = h(r_n) \times h(r_p)$. However, when obtaining the momentum and spatial distributions from the event generators, one loses the full quantum mechanical information and turns it into a semi-classical picture. Finally, using the new coordinate transformations and evaluating the p and ρ integrals Eq. 2.8 can be expressed as

$$\frac{d^3 N_d}{dP_d^3} = \frac{S}{(2\pi)^6} \int d^3 q \int d^3 r_p d^3 r_n D(r, q) G_{np}(P_d/2 + q, P_d/2 - q) h(r_n) h(r_p), \quad (2.9)$$

where $D(r, q)$ is the Wigner function of the deuteron defined in Eq. 2.5.

As stated previously, using MC simulations and the event generator, one can obtain the momentum distribution of the produced nucleons $G_{np}(p_n, p_p)$, which will include momentum correlations.

Ultimately, a probability of the formation of a deuteron from a given proton-neutron pair can be obtained by folding the deuteron Wigner function with the spatial distribution of the two nucleons,

$$P(\sigma, q) = \int d^3 r_d \int d^3 r H_{np}(r, r_d; \sigma) D(r, q). \quad (2.10)$$

This probability depends on the nucleon emission source size σ and the relative momentum q of the proton-neutron pair. It is possible to further analytically solve this equation using an ansatz for the deuteron wave function (e.g., Gaussian, Double Gaussian) or a realistic wave function (e.g., Argonne v18, χ EFT) and solve it numerically.

The *Advanced Coalescence Model* depends on the choice of the deuteron wave function. As shown in Fig. 2.4, several options are available to express it. Where *Argonne v18* wave function is obtained by fitting to most recent scattering data, for more information about the available deuteron wave functions, see Ref. [31].

This model provides a coalescence probability that relies on the distance and relative momentum of the neutron-proton pair, eliminating the need for any free parameter that would require fitting to existing data.

2. Light Nuclei production

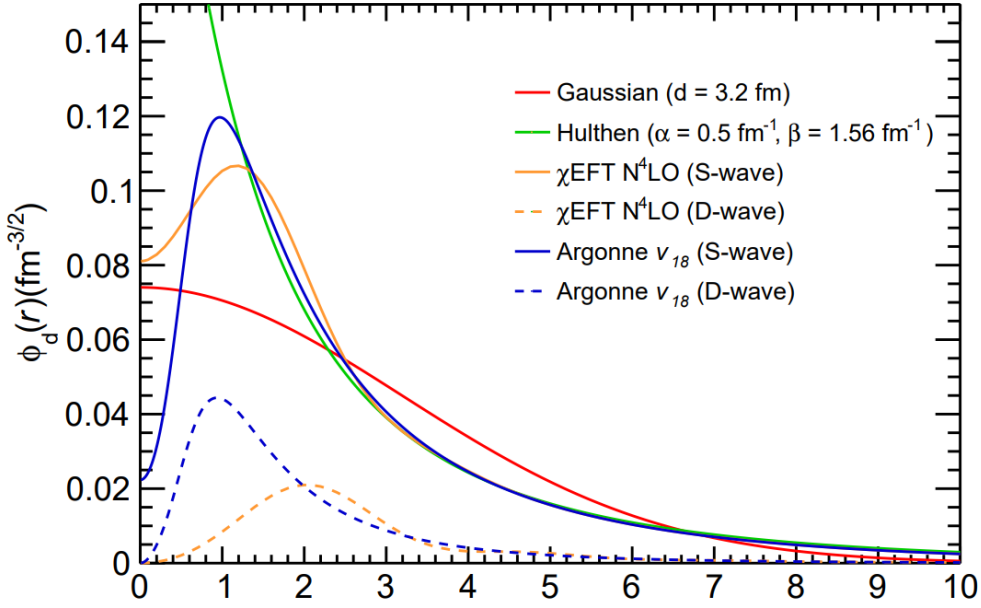


Figure 2.4.: Deuteron wave functions using different potential configurations, Gaussian (red), Hulthén (green) [32], χ EFT N^4 LO S-wave and D-wave (orange) [33] and Argonne v_{18} S-wave and D-wave (blue) [34]. Taken from [31].

2.3. Impact parameter, rapidity and charged particle multiplicity

To obtain suitable observables used to access the different stages of a HIC and allow the comparison with the predictions of theoretical models explained in Sec. 2.2, some valuable definitions are addressed in this Section, being the impact parameter of the collision, the rapidity, and the charged particle multiplicity. The graphical representation of the system coordinates is shown in Fig 2.5.

In terms of rapidity, the momentum of a particle \vec{p} can be expressed into its longitudinal momentum, \vec{p}_z and transverse momentum with module, $p_T = \sqrt{p_x^2 + p_y^2}$. The energy of the particle, E , and the angle with respect to the longitudinal direction Z is the polar angle θ . In this sense, the rapidity y and the pseudorapidity η are defined as,

$$y = \frac{1}{2} \ln \frac{E + p_z}{E - p_z} \quad (2.11)$$

$$\eta = \frac{1}{2} \ln \frac{|\vec{p}| + p_z}{|\vec{p}| - p_z} = -\ln \tan(\theta/2) \quad (2.12)$$

The impact parameter b is defined as the distance between the centers of the colliding particles, meaning central collisions are characterized by a small impact parameter, and peripheral collisions have a significant impact parameter. In Fig. 2.5, spectators are shown, those being nucleons that do not interact proceeding along their initial direction. On the other hand, participants are nucleons that interact with the nucleons of the other nucleus. These participants are left in an excited almond shape after the collision occurs.

2. Light Nuclei production

Finally, the charged particle multiplicity, often named simply multiplicity, refers to the number of charged particles produced per rapidity unit, dN_{ch}/dy . Multiplicity can be used to determine the centrality of a HIC. For central collisions, more nucleons are present in the interaction, whereas more charged particles are present. For peripheral collisions, fewer nucleon collisions and fewer charged particles are present. In this sense, higher multiplicity values mean more central collisions than lower multiplicity values assigned to peripheral collisions.

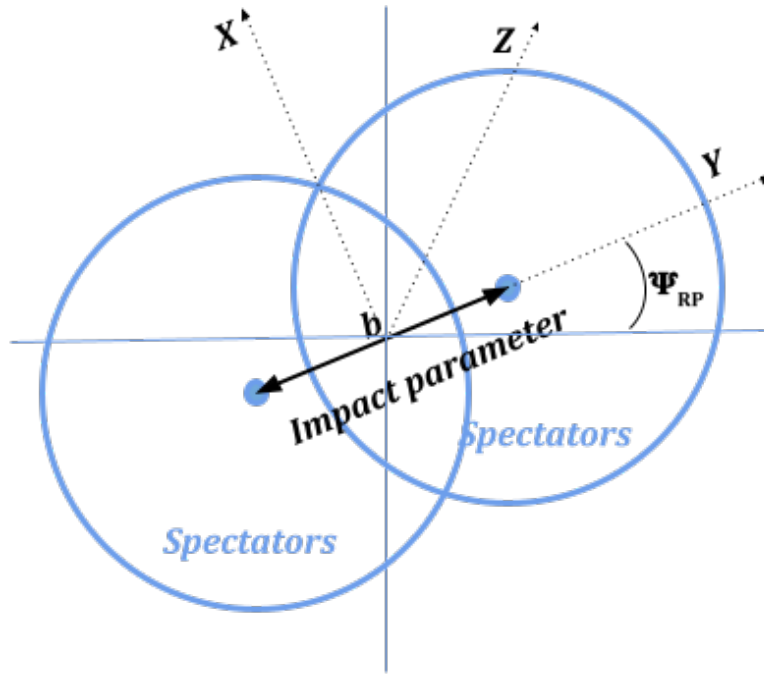


Figure 2.5.: Impact parameter b and a graphical representation of the colliding nuclei in the transverse plane. Z axis represents the beam direction while X and Y the reaction plane. The blue lines represent the lab axis with Ψ_{RP} the reaction plane angle. Adapted from [35].

3. EPOS3 Event Generator

An event generator is software used to simulate particle collisions. EPOS [36] stands for Energy conserving quantum mechanical approach, based on Partons, parton ladders, strings, Off-shell remnants, and Splitting of parton ladders. In this work, EPOS3.117 will be used; this version was developed to describe heavy-ion collisions at LHC and RHIC energies.

3.1. Working principle

In EPOS, collisions are described as colliding between a target and a projectile. If these are not single nucleons but heavy ions (e.g., Au, Pb), the distribution of nucleons inside the nucleus is determined using a Woods-Saxon potential[37]. Regge-theory describes the interaction between hadrons in EPOS [38], where the analytic properties of scattering are described as a function of angular momentum.

The elemental interaction is a parton ladder; a schematic representation is shown in Fig. 3.1a. This ladder can be seen as a longitudinal color electric field decaying into hadrons via pair production [39, 40]. Initially, multiple particles interact in parallel for heavy ion collisions, where energy is shared between the different ladders, and all ladders exist simultaneously. These parton ladders create new partons, which bind together, creating strings, as shown in Fig. 3.1b.

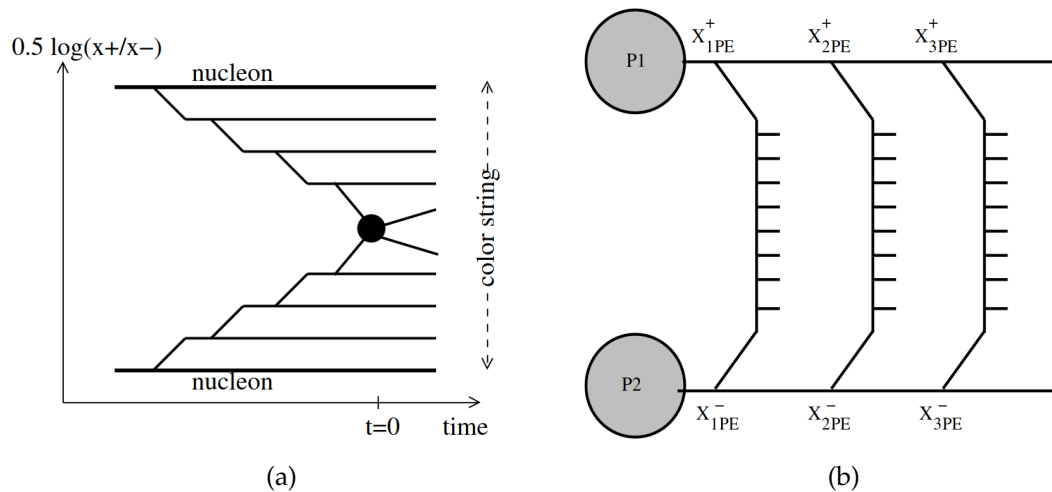


Figure 3.1.: Elementary parton-parton scattering (a). Multiple interactions between parton ladders in parallel. x_{PE} represents the fraction of total momentum for each ladder (b). Taken from [39].

3. EPOS3 Event Generator

The Schwinger mechanism between two (di-)quarks will break up these newly created strings and finally form hadrons. Diquarks are quark pairs that are not color-neutral, unlike mesons. A schematic representation of the string fragmentation mechanism is shown in Fig 3.2. Here, fragmentation points between diquarks form baryons and between quarks mesons. The hadrons created between these quarks can be even in excited states where this model implicitly conserves electric charge and baryon number.

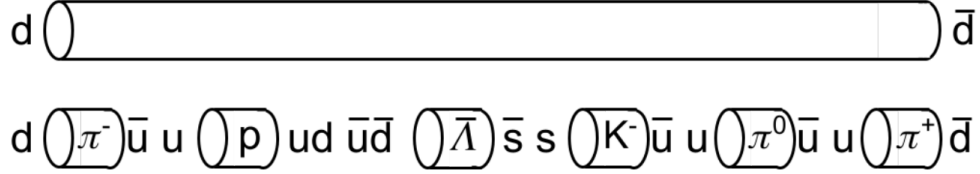


Figure 3.2.: String fragmentation mechanism between two $d\bar{d}$ forming out hadrons at each fragmentation point. Taken from [15].

For every fragment created, a transverse momentum p_T is given. If the p_T is high enough, it will be assigned to the corona, and fragments with low p_T will form the core.

As explained in Sec. 2.1, the core represents the QGP evolving using hydrodynamics. This stage is called HYDRO in EPOS. The QGP will undergo a phase transition when the energy density reaches a critical value of $\epsilon_c \simeq 1\text{GeV}/\text{fm}^3$ into a hadronized gas and expand with a decrease in temperature until the chemical freeze-out. Once this stage is reached, all particles undergo final-state interactions in the form of rescattering known as hadronic cascade and called in EPOS as HACAS carried out with the UrQMD model [41] until a kinetic freeze-out occurs. Finally, only weakly decaying particles and final-state particles are present.

3.2. Accessing EPOS

A complete simulation on an event-by-event basis is carried out in EPOS. Accessing intermediate particles and the time and momentum of creation are possible. This is a crucial aspect of the event generator and allows us to compare the early stages and the final state of the collision.

In EPOS, different event variables, particle variables, and ID codes are present to differentiate between stages explained in Sec. 3.1. Tab. 3.1 summarizes a first introduction to these variables. For each particle created in the event an index is given, following the order in which this particle is produced, meaning the first particle will have an index 1, the second index 2 in such a manner for the rest of the particles. This index can be accessed but is not directly stored. It is used in determining the mother and daughter particles of a decay.

As mentioned in Sec. 3.1, EPOS events are based on a core-corona approach, where the core is called HYDRO, and the corona is called HACAS. One can turn them off individually. This saves computational time in collisions where final stages are

3. EPOS3 Event Generator

EPOS		
Variable name	ID	Description
id	-1120, -1220, ...	particle ID in ISAJET convention ??
ist	-2, -1, 0, 1, 3, 6, 7, 8, 21, 29, 31	Status variable. Different methods
ior/jor	≥ 0	Mother particle. If the particle's primary ID is 0
zus	-999, 2, 0, >0	Mother particle if $g \neq 0$, for <0 additional purposes
x, y, z, t	No ID, position values	Four position in fm units
px, py, pz, p0	No ID, momentum values	Four momentum in GeV units
bim	≥ 0	Impact parameter of a collision or amount of pomerons

Table 3.1.: Variables used in EPOS. Multiple purposes can be accessed for different variables and IDs. Adapted from [15].

negligible for the outcome, e.g., pp collisions. There is also the possibility to turn both HYDRO and HACAS to be able to investigate initial stages, e.g., for flow studies [42].

This work will use both functionalities to study antideuteron production in Au–Au collisions. A schematic representation of the workflow used in EPOS is presented in Fig. 3.3. A list of the different stages in EPOS with the possible variables one can access is given:

- At the initial stage, particles from the projectile and the target can be accessed by identifying the position z in the positive direction. There is an offset in the x direction between the projectile and the target by half of the impact parameter of the collision. In the initial stage of the collision, the initial projectile and target have the variable $zus=-2$. If they interact with another participating nucleon, a value $ist=1$ is assigned; if this nucleon is a spectator, no interaction occurs and has a value $ist=0$.
- In the stage where parton ladders are created, EPOS gives the parton ladders an id consisting of 7 digits and ending in 99. They are assigned variables $ist=31$ and $zus=0$, and ior and jor are seen as indexes of the two nucleons that interacted, creating the parton ladder.
- Following the workflow from EPOS, free (di-)quarks and gluons are created, further creating strings. They have variables $ist=21/25$ and $zus=0$. If $ist=25$, the parton interacts by gluon emission, and if $ist=21$, there is no further interaction during this stage. The variable ior references the parton ladder where the (di-)quarks originated and jor from the parton that emitted them if they originate from an $ist=25$ parton. Otherwise $jor=0$.
- Following, a list of particles directly created, mostly in excited states, is given. They have the variables $zus=0$, $ior=0$, and $ist=3/7$. If the particle is assigned $ist=7$, it is part of the core and the hydrodynamic evolution. If $ist=3$, the particle is

3. EPOS3 Event Generator

redirected to the HACAS functionality being part of the corona. If HACAS is turned off, the particles with $ist=3$ will be assigned a value $ist=1$.

- In the string fragmentation process, strings are given an id consisting of 9 digits starting with an 8. After that, four digits for the total number of up, down, strange, and charm quarks, and the following four digits for their antiparticles. Strings have also assigned a $zus=0$ and $ist=29$, ior , and jor are given for the two (di-)quarks in the list of free quarks creating the string. The string fragments also have $zus=0$ and $ist=3/7$, depending if they are directed to HACAS with a value $ist=3$ or directed to HYDRO with $ist=7$. ior points to the string, and $jor=0$.
- At this point HYDRO stage is finished. If there is an unstable particle, its PID will be given in PDG convention [43], and the decay resulting into a stable particle will be in ISAJET convention as pointed in Tab. 3.1. If HACAS is used, particles that come out from strong decays have $ior=0$ and $zus=-999$, due to the UrQMD model not returning the mother of these particles. If HACAS is turned off, the particles will have the same zus and ior variables pointing to their mother particles. If long-lived decay resonances remain, they have $ist=1$ and final stable particles with $ist=0$.
- Additionally, both for HACAS and without HACAS a list is given with $zus=0$, $ist=6$ for particles that can decay and $ist=8$ for stable particles.
- In the end, an energy correction in terms of energy conservation is applied. This list has variables $ior=0$, $ist=-2$, and $zus=-2$.

More of the output of EPOS and all the possible stages in the workflow is shown in [42].

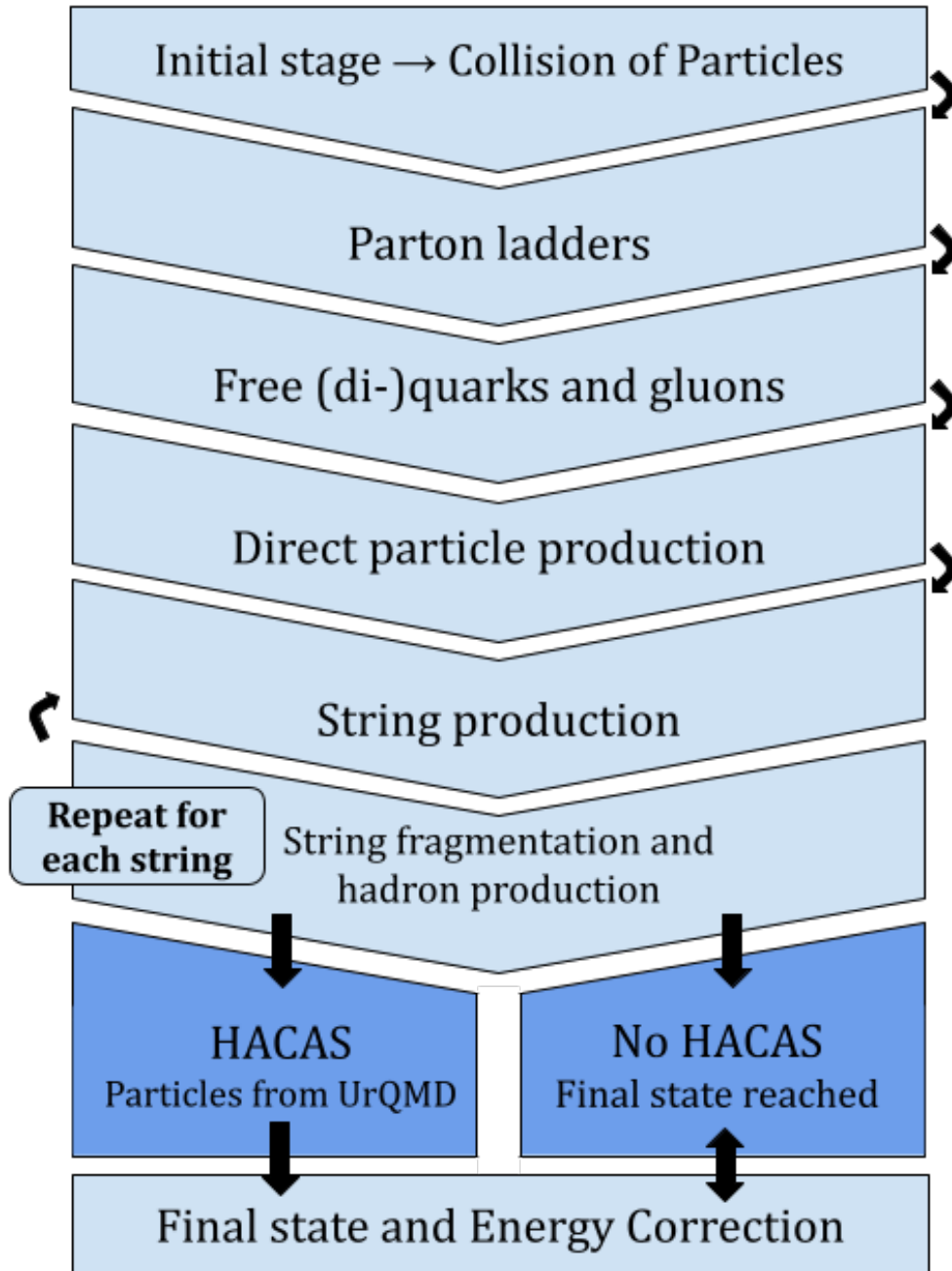


Figure 3.3.: Schematic representation of the workflow in EPOS. Adapted from [15].

4. SMASH transport model

Transport models are a primary means to extract physics information at relativistic-energy heavy-ion collisions. SMASH [44] stands for **S**imulating **M**any **A**ccelerated **S**trongly-interacting **H**adrons and is a relativistic hadronic transport model for the dynamical description of heavy-ion reactions. The later stages of a heavy-ion collision where hadronic rescattering takes place are depicted with the hadron transport approach; this stage becomes important when studying observables driven by resonance decays and baryon annihilation [45].

This section presents the SMASH approach, from general aspects to different applications. SMASH 3.0 [46] will be used in this work.

4.1. Model description

The key aspect of using a microscopic transport model is the complete availability of phase-space information at any given time. The fundamental equation used is the relativistic Boltzmann equation,

$$p^\mu \partial_\mu f_i(x, p) + m_i F^\alpha \partial_\alpha^p f_i(x, p) = C_{coll}^i \quad (4.1)$$

where m_i is the mass of the particle, C_{coll}^i is the collision term, F^α is the force single particles experience, where $F^\alpha = 0$ at high beam energy collisions and $F^\alpha = -\partial^\alpha U(x)$ for low beam energy collisions, with $U(x)$ being the mean-field potential, considered to obtain single particle states and related energy spectrum by solving the stationary Schrödinger equation, further explained in Sec. 4.1.4. Finally, $f_i(x, p)$ represents the individual particle distribution for different species i represented by test particles. These particles, in principle, are treated as Gaussian waves. In practice, one test particle represents each real particle, but more can be created; the test particle method will be further explained in the following sections. These particles' spatial extent under study is evaluated to determine thermodynamic properties like particle density.

4.1.1. Collision Criterion

In the SMASH approach, the geometrical criterion used to solve the Boltzmann equation in a relativistic environment is the one used in the UrQMD model [47], where two particles collide if their distance d_{trans} follows the relation,

$$d_{trans} \leq d_0 = \sqrt{\frac{\sigma_{tot}}{\pi}} \quad (4.2)$$

Where σ_{tot} is the total cross-section depending on the center of mass energy \sqrt{s} and the species and quantum numbers of the particles.

4. SMASH transport model

The distance between the colliding particles d_{trans} is defined as,

$$d_{trans}^2 = (\vec{r}_a - \vec{r}_b)^2 - \frac{((\vec{r}_a - \vec{r}_b) \cdot (\vec{p}_a - \vec{p}_b))^2}{(\vec{p}_a - \vec{p}_b)^2}. \quad (4.3)$$

Where a and b denote the two particles and \vec{r} and \vec{p} are the spatial and momentum coordinates in the center of the mass frame, respectively. d_{trans} corresponds to the relative distance between the two particles at the time of closest approach, where the distance d_{trans} is entirely perpendicular to the relative velocity vector of the particles. In Eq. 4.3, the total distance is expressed in the first term, and the parallel contribution to the relative velocity vector of the particles is described in the second term.

To compute the closest approach, one transforms into the local rest frame using a $6N+1$ dimensional phase space, where no time coordinates are transformed. Using the local rest frame ensures that the cross sections are calculated similarly and not depending on the reference frame of the collision.

Here, the time of the collision t_{coll} is explained as the time of the closest approach in the computational frame. The computational frame is chosen to be the equal velocity frame of the two nuclei, the same as the center of the mass frame for symmetric systems. The time t_{coll} is computed as

$$t_{coll} = -\frac{(\vec{r}_a - \vec{r}_b) \cdot (\vec{p}_a/E_a - \vec{p}_b/E_b)}{(\vec{p}_a/E_a - \vec{p}_b/E_b)^2}. \quad (4.4)$$

One needs to transform the collision times to the computational frame to distinguish the first collision for the correct ordering of the collisions.

4.1.2. Propagation

Solving the Boltzmann equation numerically needs space and time to be chosen accordingly. The time steps Δt need to be small enough for all collisions to happen and not too small to be able to perform a fast simulation.

In the model, one can choose between two options. The user defines fixed time steps, or they are dynamically determined using the information from the computed collision times. The latter method is more efficient and adapts to high and low-density regions.

We call an action any interaction between two particles. As explained in Sec. 4.1.1, if the collision satisfies the Eq. 4.2, it is added to a list of actions decaying with a time t_{coll} . After every collision is performed and sorted according to their time, an iteration over the list of actions is performed to validate every entry. The assumption used in SMASH is that there is just one interaction for each particle during a one-time step. The validation consists of evaluating that the incoming particles were not part of another action. At this point, valid actions are executed, where outgoing particles replace the incoming particles. Finally, the particles are propagated, accounting for potentials if they are present. If there is no potential present or for the later stages of the collision, SMASH works better with a dynamically determined time step.

4. SMASH transport model

4.1.3. Test particles

A method used in SMASH for overcoming locality problems and already mentioned in previous sections is using test particles. Here, all cross-sections are scaled by a factor N_{test}^{-1} and the number of initial particles is increased by the factor N_{test} ,

$$\sigma \rightarrow \sigma N_{test}^{-1} \quad (4.5)$$

$$N \rightarrow NN_{test} \quad (4.6)$$

where N_{test} refers to the test particle index, all cross sections σ and N being the initial number of particles.

These substitutions do not change the scattering rate of the collision, but the cross sections σ become smaller, changing the collision to be more local. This change in locality is re-established when $N_{test} \rightarrow \infty$. This method is also used to obtain statistics for estimating phase-space densities.

4.1.4. Mean-field Potential

As stated at the beginning of Sec. 4.1, the force experienced by the single particles is equal to the mean-field potential $U(x)$ if a low beam energy collision is present. In this scenario, the equations of motion need to change with the modified one-particle Hamiltonian,

$$H_i = \sqrt{\vec{p}_i^2 + m_{eff}^2} + U(\vec{r}_i) \quad (4.7)$$

Where m_{eff} is the effective mass of resonances and stable mass of hadrons. The effective mass is seen as the mass it seems to have when responding to forces. The corresponding equations of motion are defined as:

$$\frac{d\vec{r}_i}{dt} = \frac{\partial H_i}{\partial \vec{p}_i} = \frac{\vec{p}_i}{\sqrt{\vec{p}_i^2 + m_{eff}^2}} \quad (4.8)$$

$$\frac{d\vec{p}_i}{dt} = -\frac{\partial H_i}{\partial \vec{r}_i} = -\frac{\partial U}{\partial \vec{r}_i} \quad (4.9)$$

Finally, the potential is determined as a function of the local density [48]. These potentials are determined only after the actions are carried out at the propagation point. SMASH neglects Lorentz force and Coulomb potentials since they are negligible compared to the hadronic mean field at higher energies (RHIC/LHC).

4.1.5. Nearest Neighbor Method

One can determine if two particles will collide by evaluating the collision criterion explained in Sec. 4.1.1. To resolve all the possible collisions, every single particle must be checked for all the other particles in the system. If N represents the number of particles, the evaluation of all possible interactions will be proportional to N^2 , which is computationally heavy. To reduce the possible combinations, the space of the system

4. SMASH transport model

is divided into cells where all interactions will happen in one cell or between the neighboring cells. A more detailed explanation of the actual value for minimal cell distance and how to obtain it can be found in [44, 49].

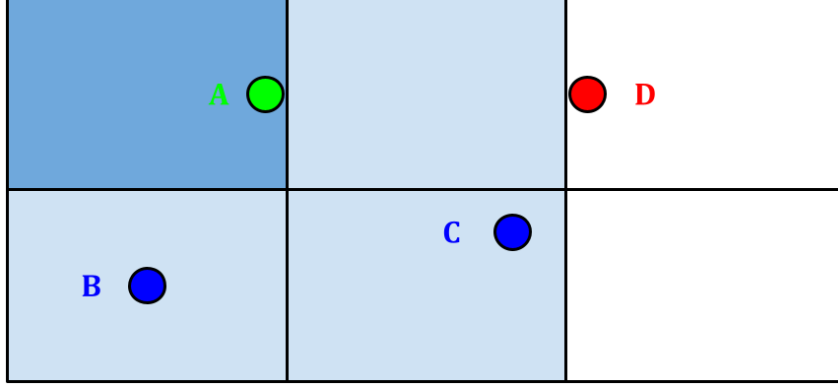


Figure 4.1.: Graphical representation in two dimensions of the cell structure to find actions between particles. Adapted from [44].

A graphical representation of the grid of cells is shown in Fig. 4.1. A differentiation is made when iterating between cells and between in-cell search. This is used to identify decays and collisions within the cell and neighbor search, where actions between particles in the cell and neighboring cells are computed. If one follows the representation shown in Fig. 4.1, the starting cell is colored in dark blue; here, actions between particle *A* and particles *B* and *C* are evaluated. If we continue onto the light blue cell, the previous dark blue cell is not taken into account since there are no more possible actions to be found. Finally, there is no action evaluation for white-painted cells since they are not neighbor cells from the starting dark blue cell.

The grid depicted is also used with periodic boundary conditions. These conditions make particles located on opposite sides of a box able to interact.

4.2. SMASH Initialization

In this section, a description of the sampling of spatial and momentum coordinates of the particles in the collision is given. Different methods on how to initialize the simulation for other purposes are explained. Further details on how to pass the input code to the SMASH transport model can be seen in their documentation in [46].

4.2.1. Nuclear Collisions

One must obtain the whole phase-space distribution to initialize the nucleons needed for a heavy-ion collision. For nuclei like Au or Pb, the spatial coordinates are determined using a Woods-Saxon distribution,

$$\frac{dN}{d^3r} = \frac{\rho_0}{e^{\frac{r-r_0}{a}} + 1} \quad (4.10)$$

4. SMASH transport model

where d is the diffuseness of the nucleus, r_0 is the nuclear radius and ρ_0 is the nuclear ground state density. At $d \rightarrow 0$, the nucleus turns into a hard sphere. For exact values and examples on different nuclei, see [44].

In Fig. 4.2, the initial positions of the nuclei are shown. In this scenario, the z -direction is the beam direction, and the $x0$ -direction represents the impact parameter direction, where the separation of the centers of the spheres is the impact parameter b . At the start the projectile P is centered in xz -direction at $(b/2, -\Delta z - \gamma_P^{-1}(R_P + d_P))$ and the target T at $(-b/2, \frac{v_T}{v_P} \Delta z + \gamma_T^{-1}(R_T + d_T))$. Where R represents the radii, d is the diffusiveness parameter, v is the absolute value of the velocity, and γ is the gamma factor.

As a condition to initialize the system, the separation between the nucleus is chosen so there are no potential influences. An additional distance $\Delta z = 2$ fm is added to evaluate all possible collisions between nucleons since the Woods-Saxon distributions give rise to a small probability of placing a nucleon at a large distance from the nucleus center. In this scenario, the initial time $t_0 = \Delta z / v_P$ is set so the projectile is constantly in motion for the target.

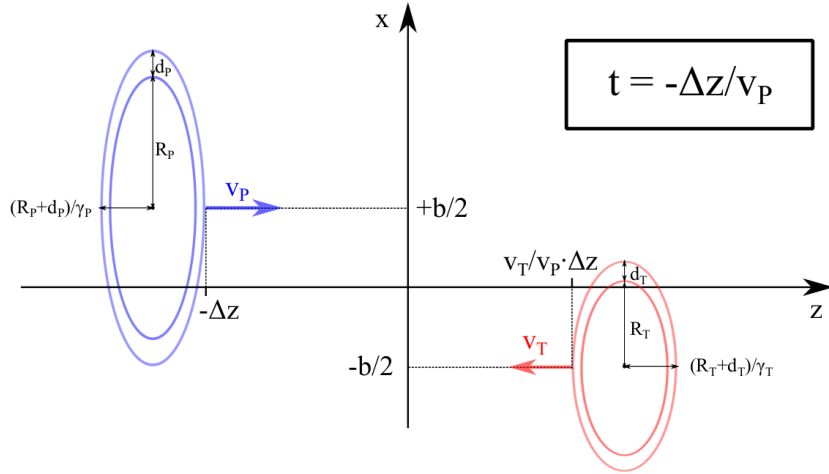


Figure 4.2.: Position of nuclei at time of initialization. The Lorentz contracted spheres will touch at $t = 0$ in a central collision. Taken from [44].

Moving now to momentum space, the nucleons of the collisions can get Fermi momenta, so a boost in z -direction is performed using the computational frame and the energy of the reaction. Here $\gamma = E_A / M_A$ of the boost, where E_A is the energy of the nucleus, M_A the mass, and A the number of nucleons. The velocity is $\beta = p_A / E_A$. The SMASH transport model accounts for the binding energy by using an approximation from the JAM transport code [50] to correctly determine the energy of the nucleus and the mass. Finally, using this premise, we obtain a boost for the momenta p'_{iz} related to the momenta of the nucleons in the rest frame of the nucleus p_{iz} ,

$$p'_{iz} = \gamma(p_{iz} + \beta E_i) = \gamma p_{iz} + \frac{p_A}{A} = \gamma p_{iz} + p_{beam} \quad (4.11)$$

where P_{beam} is the beam momentum per nucleon.

4. SMASH transport model

4.2.2. Infinite matter

Another way of initializing the simulation is to assume infinite hadronic matter or other simple systems like an ideal massive or massless gas to access thermodynamic information. This is done with box calculations. Then, N number of particles with species i is placed inside a box with length L . For each particle j , with spatial coordinates (x_j, y_j, z_j) , four-momentum E_j, \vec{p}_j and a spectral function, a distribution U is initialized. This distribution is uniform and the N particles inside the box are initialized accordingly with coordinates $x_j = U(0, L)$, $y_j = U(0, L)$ and $z_j = U(0, L)$. In this sense, the momenta of the particles are determined using the thermal Boltzmann distribution with a temperature T here, a probability $w(p)$ is given to the momentum generation p depending on the angles in spherical coordinates and a normalization factor:

$$w(\vec{p}) = N \exp(-\sqrt{\vec{p}^2 + m^2}/T) p^2 dp \sin\theta d\theta d\phi. \quad (4.12)$$

At the starting point, the particles are propagated, colliding with each other. The box depicted has periodic boundaries, and the simulation is carried with a time-step and a grid of cells as explained in Sec. 4.1.2.

4.2.3. Expanding sphere

Analogously to the previous section, a simple simulation can be carried out using a sphere with a radius R . The momenta is sampled similarly to the thermal Boltzmann distribution, and the system expands without constraints. This option for the simulation is usually used to compare with analytic solutions.

4.2.4. Afterburner

The last initialization possibility is to use as input a predefined particle list. In this scenario, the list of particles does not require an equal time in the computational frame since consecutive particles are carried by evaluating them at non-zero formation times.

This method usually addresses the later stages of heavy-ion collisions at high beam energies, dominated by hadronic rescattering and resonance decays.

An example on how to initialize such configuration in SMASH and how the list of predefined particles looks like can be found in Appendix A.

5. Beam Energy Scan Program

The Beam Energy Scan (BES) program [51] was initiated in 2010 at the Relativistic Heavy Ion Collider (RHIC) located at the Brookhaven National Laboratory. The program is aimed to investigate the phase diagram of strongly interacting nuclear matter. The BES program has different phases; BES phase I (BES-I) was completed in 2011 with Au–Au collisions in the energy range of 200 GeV to 7.7 GeV and introduced phase transition signatures and the critical point of the Quantum Chromodynamics (QCD) phase diagram, explained later in this Chapter. Further improvement of the BES program in 2015 comes with implementing a fixed-target mode of data taking to collision energies below 7.7 GeV. Finally, the BES phase II (BES-II) is an ongoing experiment that provides data sets with more extensive statistics at collision energies below 3.0 GeV. All these data sets are collected by the STAR (Solenoidal Tracker at the RHIC) detector [52].

The main aspects searched at the BES program include signatures for the first-order phase transition where finite size effects can modify the behavior, the critical point of the QCD phase diagram where fluctuations at the vicinity of the critical point are studied, and the deconfinement phase where a change from different states is examined. Figure 5.1 shows the QCD phase diagram with the RHIC energies from the different BES phases.

5.1. QCD Phase diagram

QCD is the gauge field theory within the Standard Model that describes the strong interaction of quarks and gluons, the fundamental microscopic degrees of freedom [53]. This theory describes the behavior of matter from QGP to compact stars.

The phase diagram is used to express the thermodynamic properties of the system, in the case of QCD, in terms of the temperature T and the baryon chemical potential μ_B . Each point of the phase diagram represents a stable state, described by numerous thermodynamic functions like pressure, baryon density, diffusion, viscosity, etc. [54]. A graphical representation of the QCD phase diagram can be seen in Fig. 5.1. Here, the first-order transition line between the two coexisting phases, hadron gas and QGP ends at a second-order critical point.

The QCD vacuum is represented as the origin of the QCD phase diagram. Nuclei are located at $T \approx 0$ and $\mu_B \approx 1\text{GeV}$. Moving along the μ_B axis, a transition to a deconfined state is expected from theoretical models. Around $\mu_B \approx 5\text{GeV}$, this state is expected at the core of neutron stars [55]. The Hadron Gas phase is present for $\mu_B \lesssim 1\text{ GeV}$. We find conditions similar to those in the early universe for large T and $\mu_B \approx 0$. These conditions are probed by the high energies of the BES program (200 GeV, 130 GeV) and at the LHC at 2.76 and 5.02 TeV shown in Fig. 5.1 for the Phase diagram as purple, blue, and orange lines. Increasing temperature increases the mean transferred

momentum, making the strong interaction less intense [16]. The transition from the QGP to the hadronic matter happened at $\mu_B \approx 0.33$ eV [56]. The first-order phase transition from confined to deconfined strongly interacting matter is expected at high μ_B . For $\mu_B \approx 0\text{GeV}$, a crossover transition is expected at the $T \approx 160$ MeV [57]. The critical point is a singularity on the phase diagram at the end of the first-order phase transition. This critical point is expected to be at $T \approx 160$ MeV, but for μ_B many models using Monte Carlo simulations and lattice predictions find the location of the critical point to be at $0 < \mu_B < 1600$ MeV [54].

5.2. STAR Experiment

The STAR detector located at the RHIC comprises many particle identification and tracking subsystems [58]. In Fig. 5.2, a graphical representation of the STAR detector and its systems is shown. These subsystems include a room-temperature solenoidal magnet for charged particle momentum analysis, a Silicon Vertex Tracker (SVT) and Silicon Strip Detectors (SSD) for charged particle tracking, a Time Projection Chamber (TPC) is used to record the collisions and identify particles with momenta greater than 100 MeV/c. Both TPC and SVT accomplish particle identification using the dE/dx method [59], a Forward Time Projection Chamber (FTPC) to extend the tracking in the forward region, a Barrel Electromagnetic Calorimeter (BEMC) is used to study high p_T processes like heavy quarks, jets, etc. and provide excellent event characterization in heavy-ion collisions [60], a Time-Of-Flight detector (TOF) is used to distinguish particles using the velocity the particle takes to travel through the detector, a data acquisition system (DAQ) and a triggering system to control the event selection.

Three central studies can be divided for the STAR experiment: the measurement of the spin structure function of the proton, the survey of high-density QCD, and photon pomeron interactions from electromagnetic fields.

STAR studies proton-nucleus and proton-proton interactions to investigate the incident nuclei's parton distribution functions and acquire data for heavy ion studies. By looking into polarized proton interactions, the STAR experiment can determine how much the proton's overall spin is affected by the orientation of gluon spins and allows one to choose the flavor dependence on antiquark polarizations [61].

Concerning the studies for a high-density QCD, the freezeout geometry of the collision, the expansion scheme, and the possible existence of a QGP are investigated with correlations between identical and non-identical particles [62].

With the help of STAR data, it was possible to calculate hard scattering using perturbative quantum chromodynamics (pQCD). This allowed for high transfer momentum processes present as high p_T jets, single particles, etc., to determine the properties of the medium through which they propagate.

5. Beam Energy Scan Program

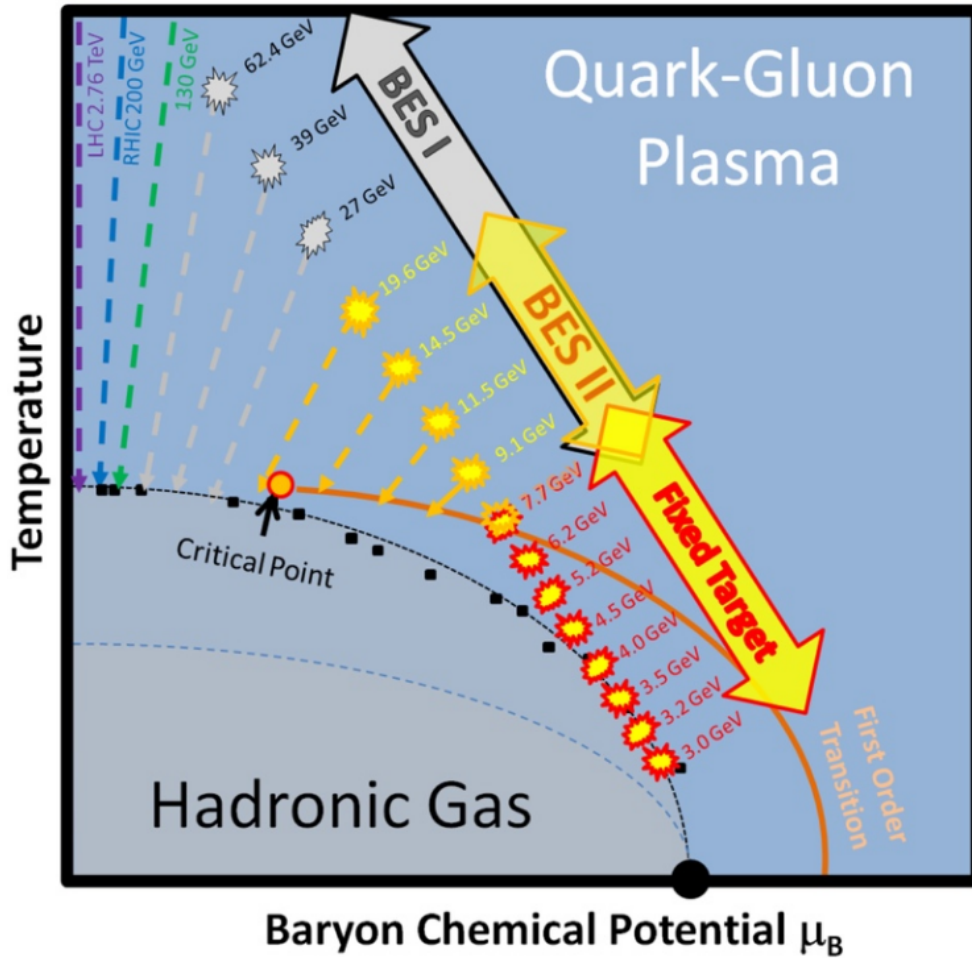


Figure 5.1.: The QCD phase diagram with RHIC energies performed during the BES program and LHC energy at 2.76 TeV is shown in purple. Two energies at 200 GeV and 130 GeV from RHIC are shown in green and blue, respectively. The energies from the first phase of BES are shown in grey (62.4 GeV - 27 GeV). The second phase of the BES is presented in yellow for energies between 19.6 GeV and 7.7 GeV. Finally, the energies performed during the fixed target experiment are shown in red from 7.7 GeV to 3.0 GeV. The presented energies allowed to scan μ_B from 400 MeV to 20 MeV. At the top energies, the QCD calculations predict a cross-over transition with $T \approx 150 - 170$ MeV and $\mu_B \approx 0$ GeV. The first-order transition is present for lower T and higher μ_B for the right side energies. The red line represents the phase transition with its endpoint, the QCD critical point shown in a red circle. Taken from [51].

5. Beam Energy Scan Program

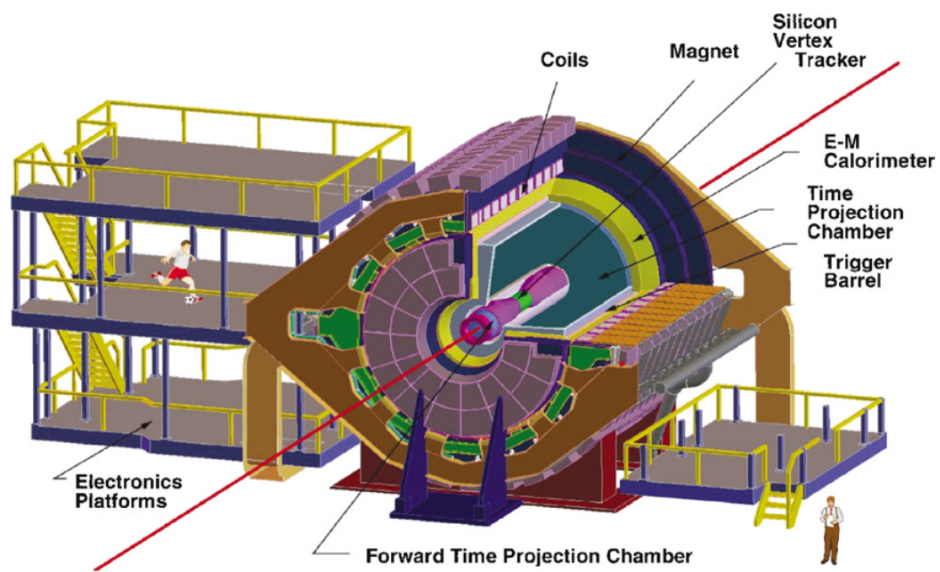


Figure 5.2.: Perspective view of the layout of the STAR Experiment. A cutaway is present to see the inner detector systems. Taken from [58].

6. Correcting the Event Generator

As stated in Sec. 1, one of the motivations for understanding the (anti-)nuclei production and cosmic-ray antiparticles is that those can be seen as messengers for processes such as dark-matter decays and annihilation with a low astrophysical background [63]. This work studies the energy regime $\sqrt{s} \sim GeV$ probed by the STAR experiment in Au–Au collisions. Compared to $\sqrt{s} \sim TeV$ at the LHC, the STAR experiment is more suitable because the peak in the production of nuclei for cosmic rays is $\sim 30 GeV$. A study at energies of $\sqrt{s_{NN}} = 200 GeV$ and $\sqrt{s_{NN}} = 62.4 GeV$ gives rise to better statistics compared to lower energies, and it is suitable to test the models with event generators.

This Chapter presents a correction scheme in Sec. 6.1 to tune the event generator. In Sec. 6.2, a comparison between charged particle multiplicities from the STAR experiment and the event generators is performed to choose consistent centrality classes. A study on the antiproton and antineutron spectra will also be needed to correct discrepancies between the event generators and the data, presented in Sec. 6.4. Finally, to address a correct antideuteron production, the event generators need to be tuned to the source size of the collision; here, again, a comparison between values of data from the STAR experiment and the event generators will be made in Sec. 6.3. To model (anti-)deuteron production, two EPOS simulations at the nucleon-nucleon center-of-mass energy of $\sqrt{s_{NN}} = 62.4$ and $200 GeV$ were produced with $\sim 3 \cdot 10^6$ events. In both productions, the full functionality of EPOS, where HYDRO and HACAS are used. For SMASH, the transport model initializes a list of all predefined particles obtained after the HYDRO stage in EPOS for a similar production of Au–Au collisions at the nucleon-nucleon center-of-mass energy of $\sqrt{s_{NN}} = 200 GeV$, with $\sim 500 \cdot 10^3$ events.

6.1. Correction Scheme

A correction on an event-by-event basis is applied to tune the event generators. In this sense, every event or particle present in the production is weighted with a factor previously determined. The way to obtain this correction factor is done by comparing the prediction from the event generators to the measured experimental data by STAR.

This correction scheme is presented as,

$$\left(\frac{f_{Data}}{f_{prediction}} \right) \cdot f_{prediction} = f_{correction\ factor} \cdot f_{prediction} = f_{Data}. \quad (6.1)$$

The data obtained is presented in bins, in terms of multiplicity and source size by different centrality classes and for momentum distributions in $m_T - mp$ spectra for the productions at $200 GeV$ and p_T for $62.4 GeV$. A bin-by-bin correction will be applied for the first two. An event-by-event method is used for the momentum distributions,

6. Correcting the Event Generator

Au–Au 200 GeV		Au–Au 62.4 GeV	
Centrality	$\langle N_{ch}/dy \rangle$	Centrality	$\langle N_{ch}/dy \rangle$
70-80%	26.5 ± 1.8	70-80%	17.7 ± 1.3
60-70%	52.1 ± 3.5	60-70%	35.8 ± 2.8
50-60%	90.2 ± 6.0	50-60%	65.0 ± 5.0
40-50%	146 ± 10	40-50%	107 ± 8
30-40%	222 ± 15	30-40%	166 ± 11
20-30%	337 ± 23	20-30%	249 ± 16
10-20%	484 ± 33	10-20%	359 ± 24
5-10%	648 ± 44	5-10%	476 ± 30
0-5%	811 ± 56	0-5%	582 ± 38

Table 6.1.: Summary of centralities in Au–Au collisions at 200 GeV and 62.4 GeV regarding mean multiplicity rapidity density in the rapidity region of $|y| < 0.1$. The total errors are obtained from summing statistical and systematic uncertainties in quadrature. Adapted from [64].

meaning each event or particle in phase space is given a unique correction factor. This will be done using a linear fit, further explained in Sec. 6.4.

6.2. Charged Particle Multiplicity

In this section, a summary of mean charged particle multiplicity rapidity density, $\langle N_{ch}/dy \rangle$, obtained by the STAR Collaboration [64] is shown in Tab. 6.1. These values are presented as a function of centrality where the identified charged particle spectra are formed from π^\pm , K^\pm , \bar{p} and p . The measurement is presented with nine centrality classes (0-5%, 5-10%, 10-20%, 20-30%, 30-40%, 40-50%, 50-60%, 60-70%, and 70-80%) and is measured at mid-rapidity with a rapidity cut in $|y| < 0.1$.

To obtain consistent centrality classes from the event generator, one can get a distribution of charged particles per event and determine the limits of the centrality classes by how much percentage they represent in terms of the total number of events; an example of how to obtain the multiplicity limits is shown in Fig. 6.1 for the EPOS productions. The same procedure is applied when getting the centrality classes from SMASH.

In this sense, the mean values for the multiplicity are obtained and compared to values from the STAR experiment shown in Tab. 6.1.

In Fig. 6.2, a comparison between EPOS and SMASH mean multiplicity values to the STAR-measured results at 200 GeV is shown. The picture shows that EPOS and SMASH cannot reproduce high multiplicity values and lay below the measured data by a factor of ~ 0.9 for EPOS and ~ 0.8 for SMASH. For lower multiplicities and more peripheral events, EPOS predicts higher multiplicities than the measurement data by a factor of ~ 1.1 , while SMASH prediction is by a factor of ~ 1.3 . At semicentral events, both EPOS and SMASH can reproduce the multiplicities from the STAR Data with minor differences.

In Fig. 6.3, a comparison between EPOS multiplicity values and STAR-measured

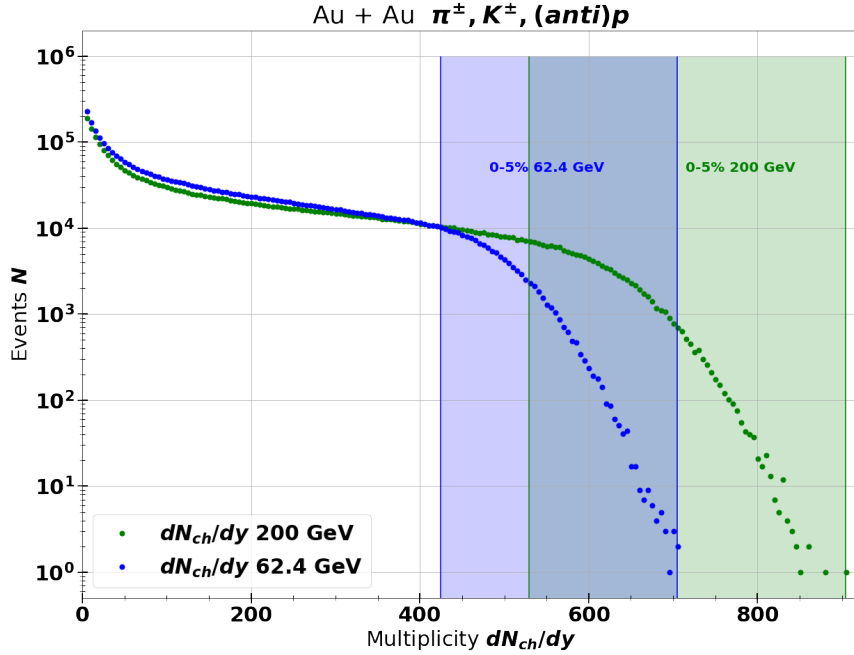


Figure 6.1.: Charged particle distributions obtained with EPOS at 200 GeV (green) and 62.4 GeV (blue). The green and blue bands represent the 5% most central events for the multiplicity distributions at 200 GeV and 62.4 GeV, respectively. Both distributions for the multiplicity rapidity density are obtained with a rapidity slice of $|y| < 0.1$, similar to the STAR data.

results at 62.4 GeV is shown. Like the distributions at 200 GeV, EPOS cannot reproduce high multiplicity values and lays below the measured data by a factor of ~ 0.8 . For lower multiplicities, EPOS predicts larger ones than the data by a factor of ~ 1.1 . The best-predicted values lay at 40% - 60% centrality, where EPOS can reproduce almost perfectly the data obtained by STAR. These disparities will be corrected and considered when evaluating the multiplicity to get suitable centrality classes to evaluate both antiproton production and source size measurements.

6.3. Source Size

As explained in Sec. 2.2.2, the probability of forming an (anti-)deuteron from a given pair of (anti-)proton-(anti-)neutron depends on the relative momentum of the pair and the source size, which is a measure for the distance between all possible antiproton-antineutron pairs of the collision. More particles collide for central events, and the geometrical overlap is bigger than for peripheral events with more spectators. It is crucial to obtain a suitable source size from the event generators and correct it to data at different energies and centrality classes to address the deuteron wave function and the probability of obtaining one. This work assumes $\mathbf{p} - \mathbf{p}$ source size is the same as

6. Correcting the Event Generator

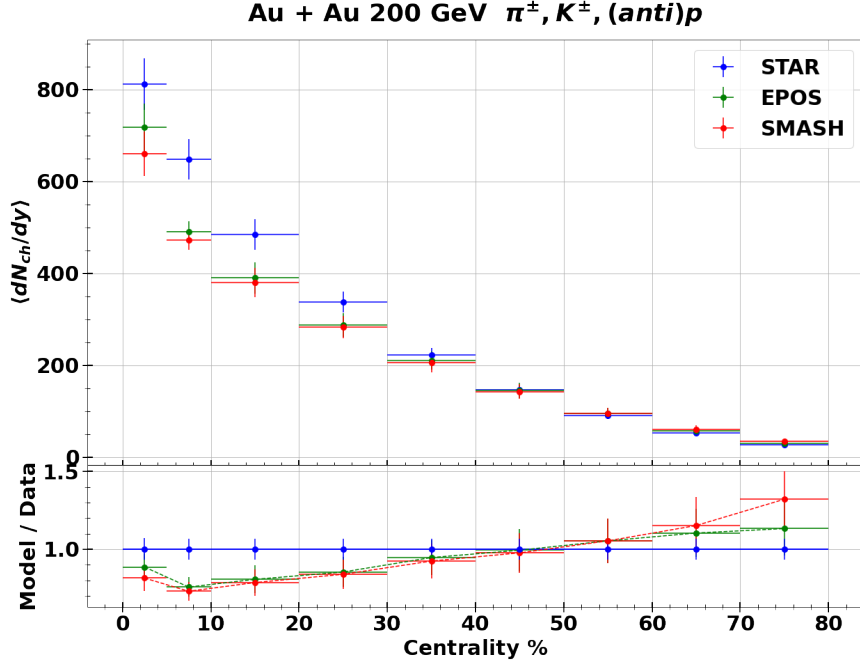


Figure 6.2.: Comparison of the mean multiplicity rapidity density, $\langle N_{ch}/dy \rangle$, at 200 GeV for STAR data (blue), EPOS (green), and SMASH (red).

$\mathbf{p} - \mathbf{n}$ due to Isospin symmetry. This assumption is needed since the STAR experiment does not measure neutrons.

Tab. 6.2 presents values for the source size from Au–Au collisions at 200 GeV and 62.4 GeV for three different centrality classes, obtained from the STAR Collaboration [65]. The different centrality classes are obtained as explained in Sec. 6.2 to get suitable values for the source size from the event generators. At 200 GeV $\bar{\mathbf{p}} - \bar{\mathbf{p}}$ correlations were used to account for the source size. These are compatible within uncertainties with the values from $\mathbf{p} - \mathbf{p}$ correlations at 200 GeV. At 62.4 GeV, no experimental data is present for $\bar{\mathbf{p}} - \bar{\mathbf{p}}$ correlations, so $\mathbf{p} - \mathbf{p}$ correlations are used.

To obtain the source size from the Event Generator to compare with experimental values shown in Tab. 6.2, distance distributions of antiproton-antiproton pairs at 200

Au–Au 200 GeV			Au–Au 62 GeV	
Centrality	$\bar{\mathbf{p}} - \bar{\mathbf{p}}$	$\mathbf{p} - \mathbf{p}$	Centrality	$\mathbf{p} - \mathbf{p}$
0-10%	5.2 ± 0.2	4.2 ± 0.2	0-10%	4.2 ± 0.5
10-30%	4.0 ± 0.3	3.8 ± 0.3	10-30%	3.2 ± 0.3
30-80%	2.6 ± 0.2	2.7 ± 0.2	30-80%	2.5 ± 0.3

Table 6.2.: Summary of source sizes (in fm) in Au–Au collisions at 200 GeV and 62.4 GeV regarding antiproton-antiproton and proton-proton correlations. The total errors are formed of statistical uncertainties. Adapted from [65].

6. Correcting the Event Generator

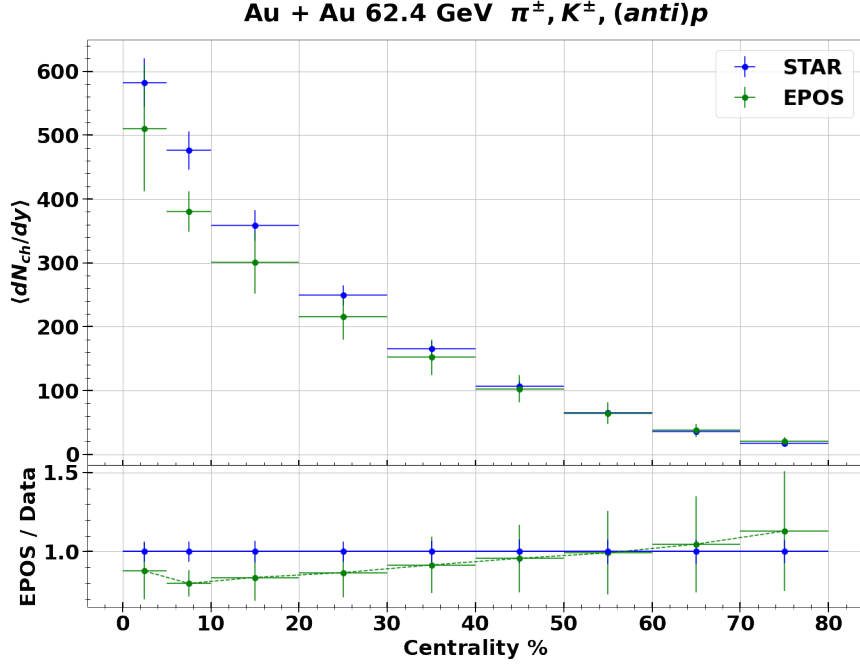


Figure 6.3.: Comparison of the mean multiplicity rapidity density, $\langle N_{ch}/dy \rangle$, at 62.4 GeV for STAR data (blue) and EPOS (green).

GeV are obtained from the event generators from EPOS and SMASH productions. For the simulation at 62.4 GeV, the distance between proton-proton pairs is obtained to compare with STAR Data. Fig. 6.4 shows different distance distributions at 0-10 % centrality between antiproton and proton pairs. These distributions follow a Gaussian source with exponential tails due to long-lived resonances and can be fitted using a Gaussian function to obtain the source size, σ as:

$$N \cdot \frac{4\pi x^2}{(4\pi\sigma^2)^{3/2}} e^{-\frac{x^2}{4\sigma^2}} \quad (6.2)$$

Where x represents the distance between the pairs, σ is the source size, and N is a normalization factor needed for the distribution to be normalized to 1 since the exponential tail from the resonances makes the Gaussian source imperfect. Using this approach, one can obtain the source size σ values from the event generators for different centrality classes.

In this work, the target centrality classes to obtain the final antideuteron yields, presented in Chapter. 7 are 0-10 %, 10-20 %, 20-40 %, 40-60%, and 60-80%. An interpolation from the source sizes shown in Tab. 6.2 is done to obtain values from the STAR Data at these centrality classes. As explained earlier in this section, the source size scales with the multiplicity and, more precisely, with the cube root of the multiplicity. In Fig. 6.5b at 200 GeV and Fig. 6.6b, the source radii from STAR are presented against the cube root of the multiplicity, $(dN_{ch}/d\eta)^{1/3}$. In this sense, an interpolation is done

6. Correcting the Event Generator

to obtain the STAR source radii at the different target centralities.

A comparison of the interpolated values to the ones from EPOS is shown in Fig. 6.5a at 200 GeV and Fig. 6.6a at 62.4 GeV to correct the event generators.

In Fig. 6.5a, EPOS and SMASH produce source sizes 40% smaller than the STAR data for central and mid-central events. At 40% centrality, the source radii for EPOS and SMASH are compatible within errors in STAR data. For peripheral events, the source size obtained from the event generators is 50% bigger than the one presented by STAR.

In Fig. 6.6a, EPOS produces source sizes compatible with the STAR data for central and mid-central events. From 30% centrality to the most peripheral events, the source radii obtained from EPOS compared to the values from STAR data are up to 30% bigger at 60-80% centrality.

The ratios presented at the bottom for both figures between the values from STAR and the models will be used to correct the event generators to get suitable source sizes as explained in Sec. 6.1.

After correction, the source size produced by EPOS and SMASH is shown in Fig. 6.7. EPOS simulations at 200 and 62.4 GeV match the experimental data. For SMASH, the source size produced after correction is 10% off for peripheral events, but the values are within uncertainties.

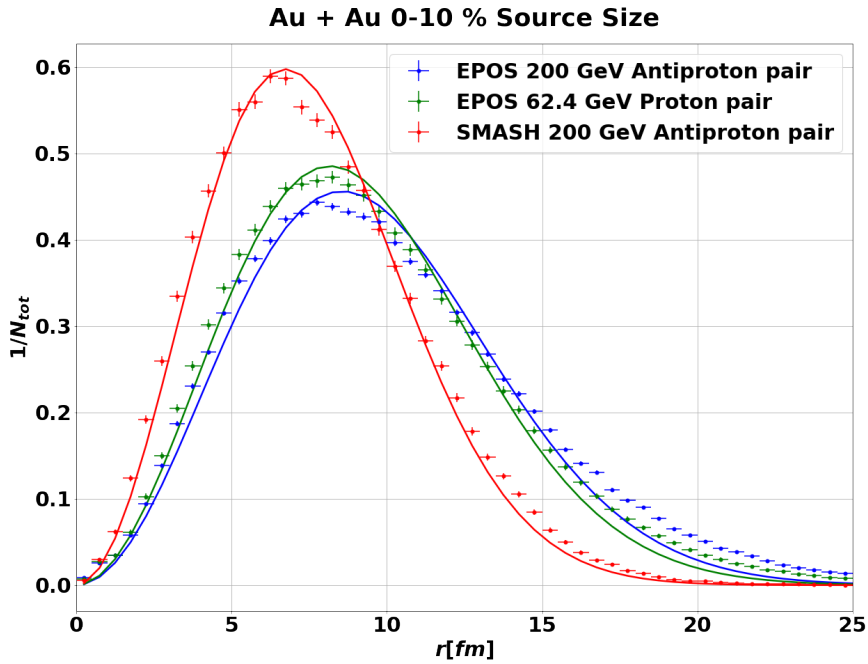


Figure 6.4.: Distance distributions at 0-10 % centrality normalized to the total number of events for antiproton pairs at 200 GeV obtained from EPOS (blue) and SMASH (red). The green points represent the distance between proton pairs at 62.4 GeV for a 0-10 % centrality. The curves are fit using Eq. 6.2 assuming a Gaussian Source.

6. Correcting the Event Generator

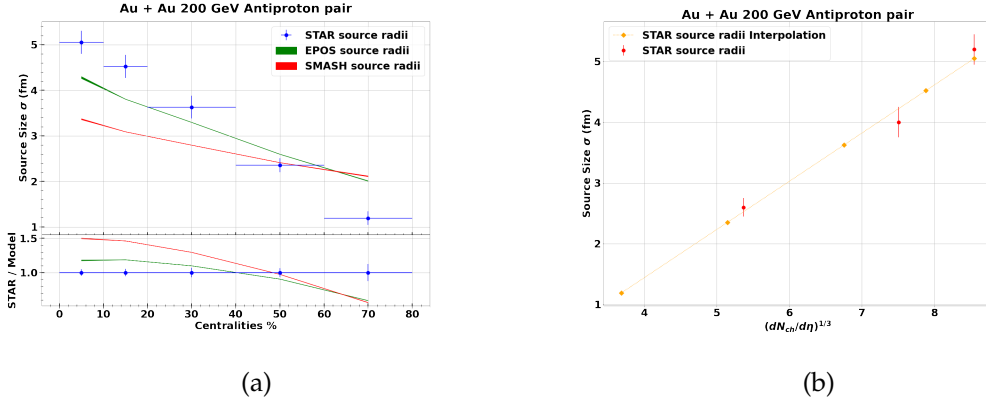


Figure 6.5.: Antiproton pair source radii at 200 GeV for different centrality classes obtained from EPOS (green) and SMASH (red) compared to STAR Data (blue) (a). Source radii from STAR (red) against $(dN_{ch}/d\eta)^{1/3}$. An interpolation is performed along the dashed orange line, with the new source radii (orange) at 5 different centralities (b).

In Fig. 6.8, it is shown how the source size scales with values for the transverse mass m_T , a comparison between the three simulations is done at three different m_T bins (1.0-1.15, 1.15-1.3, 1.3-1.6 GeV) at five different centralities. Similar behavior for the m_T scaling is observed for the different productions.

6.4. Momentum Distributions

Similar to the previous section, a correction for producing antiproton and antineutron pairs is needed to obtain the correct ones to form antideuterons. The antiproton yields obtained experimentally from the STAR Collaboration at 200 GeV [66] and 62.4 GeV [64] are compared to predictions of antiproton production spectra from EPOS and SMASH.

In Fig. 6.9, $m_T - m_p$ spectra for a 200 GeV Au–Au collision at 0-5 % centrality are obtained for EPOS and SMASH and production before the hadronic phase to compare the behavior after applying both event generators and with the STAR Data. As expected, the antiproton yield computed before the hadronic stage is much higher than the experimental data for lower m_T bins. After applying the SMASH afterburner, the $m_T - m_p$ spectra are scaled down with a similar shape compared to the production before the Hadronic phase. On the other hand, EPOS changes the shape and scales down the $m_T - m_p$ spectra for antiprotons. The resulting spectra are similar in shape to the measurement. At the bottom of Fig. 6.9, the ratios between the models and the data obtained by the STAR Collaboration are presented. The ratios give a linear behavior when compared with the experimental data. A linear fit is performed for both models at different centralities to obtain a suitable correction for the event generators. For EPOS, the linear fit is relatively flat due to the similarity in shape with the experimental data. The shape deviates from STAR data for SMASH, and the linear fit presents a significant slope.

6. Correcting the Event Generator

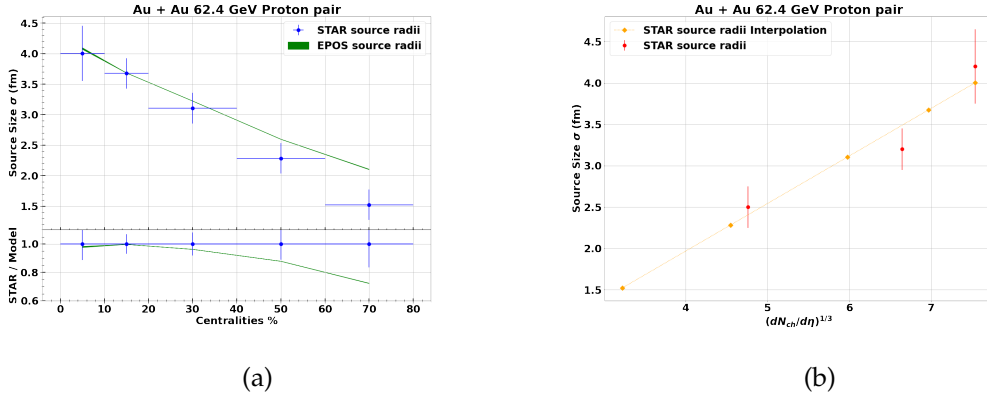


Figure 6.6.: Proton pair source radii at 62.4 GeV for different centrality classes obtained from EPOS (green) compared to STAR Data (blue) (a). Source radii from STAR (red) against $(dN_{ch}/d\eta)^{1/3}$. An interpolation is performed along the dashed orange line, with the new source radii (orange) at 5 different centralities (b).

The linear fit used to correct the event generators is expressed as,

$$y = a \cdot x + b, \quad (6.3)$$

where y represents the yield points and x the $m_T - m_p$ spectra. A complete description of all the fits used in EPOS at 200 GeV is shown in Tab. 6.3 and for SMASH at 200 GeV in Tab. 6.4. For the production at 62.4 GeV, the fits used for EPOS are shown in Tab. 6.5.

After computing the correction using the previously mentioned linear fit for the different centralities and models, the corrected antiproton yields compared to the experimental data from STAR are presented in Fig. 6.10 for an EPOS production at 200 GeV, Fig. 6.11 for SMASH at 200 GeV and Fig. 6.12 for EPOS at 62.4 GeV. Using the coalescence model, these tunings and linear fits will correct the (anti-)deuteron yields for the event generator's shortcomings in producing nucleon momentum distributions. Similarly, the antineutron yields are obtained from models and corrected to STAR data, as described in this section. This correction also corrects the multiplicity classes where the event generators cannot produce sufficient charged particles as the experimental data.

6. Correcting the Event Generator

Au–Au 200 GeV EPOS				
Centrality	Fit Antiproton	χ^2	Fit Antineutron	χ^2
70-80%	-0.02695 x + 1.152	$1.70 \cdot 10^{-2}$	-0.127 x + 1.302	$4.39 \cdot 10^{-2}$
60-70%	0.1766 x + 1.025	$1.12 \cdot 10^{-2}$	0.0587 x + 1.091	$8.61 \cdot 10^{-3}$
50-60%	0.06587 x + 0.999	$5.79 \cdot 10^{-3}$	0.02115 x + 1.011	$6.70 \cdot 10^{-3}$
40-50%	0.07451 x + 0.9297	$2.33 \cdot 10^{-3}$	0.05475 x + 0.9165	$5.42 \cdot 10^{-3}$
30-40%	-0.04371 x + 0.9105	$6.17 \cdot 10^{-3}$	-0.06141 x + 0.8815	$5.01 \cdot 10^{-3}$
20-30%	-0.09092 x + 0.8397	$2.21 \cdot 10^{-3}$	-0.103 x + 0.8084	$1.62 \cdot 10^{-3}$
10-20%	-0.1472 x + 0.7999	$2.59 \cdot 10^{-3}$	-0.1406 x + 0.7529	$2.67 \cdot 10^{-3}$
5-10%	-0.09037 x + 0.7425	$2.33 \cdot 10^{-3}$	-0.0682 x + 0.6891	$3.02 \cdot 10^{-3}$
0-5%	-0.135 x + 0.7327	$8.80 \cdot 10^{-4}$	-0.1005 x + 0.6602	$1.77 \cdot 10^{-3}$

Table 6.3.: Summary of antiproton and antineutron fits in Au–Au collisions at 200 GeV for EPOS.

Au–Au 200 GeV SMASH				
Centrality	Fit Antiproton	χ^2	Fit Antineutron	χ^2
70-80%	-0.4275 x + 1.211	$7.40 \cdot 10^{-2}$	-0.778 x + 1.543	$1.90 \cdot 10^{-1}$
60-70%	-0.4163 x + 1.066	$3.87 \cdot 10^{-2}$	-0.5447 x + 1.219	$2.42 \cdot 10^{-2}$
50-60%	-0.5092 x + 0.9941	$2.16 \cdot 10^{-2}$	-0.6776 x + 1.136	$2.26 \cdot 10^{-2}$
40-50%	-0.5286 x + 0.9709	$1.60 \cdot 10^{-2}$	-0.7104 x + 1.077	$1.10 \cdot 10^{-2}$
30-40%	-0.6777 x + 0.9715	$8.83 \cdot 10^{-3}$	-0.7719 x + 1.053	$1.16 \cdot 10^{-2}$
20-30%	-0.7932 x + 0.9632	$8.88 \cdot 10^{-3}$	-0.9094 x + 1.032	$1.82 \cdot 10^{-2}$
10-20%	-0.8561 x + 0.9414	$9.85 \cdot 10^{-3}$	-0.9757 x + 1.001	$9.14 \cdot 10^{-3}$
5-10%	-0.8421 x + 0.9087	$8.19 \cdot 10^{-3}$	-0.9163 x + 0.9492	$1.35 \cdot 10^{-2}$
0-5%	-0.9363 x + 0.936	$1.03 \cdot 10^{-2}$	-0.8946 x + 0.9074	$9.30 \cdot 10^{-3}$

Table 6.4.: Summary of antiproton and antineutron fits in Au–Au collisions at 200 GeV for SMASH.

Au–Au 62.4 GeV EPOS				
Centrality	Fit Antiproton	χ^2	Fit Antineutron	χ^2
70-80%	-0.2194 x + 1.881	$2.33 \cdot 10^{-2}$	-0.2779 x + 2.188	$8.25 \cdot 10^{-2}$
60-70%	-0.06433 x + 1.382	$2.52 \cdot 10^{-2}$	-0.1605 x + 1.546	$1.71 \cdot 10^{-2}$
50-60%	0.1045 x + 1.185	$1.54 \cdot 10^{-2}$	0.0216 x + 1.252	$1.66 \cdot 10^{-2}$
40-50%	0.09103 x + 1.079	$7.10 \cdot 10^{-3}$	0.02402 x + 1.095	$7.99 \cdot 10^{-3}$
30-40%	-0.008131 x + 1.027	$6.02 \cdot 10^{-3}$	-0.03907 x + 0.9997	$5.27 \cdot 10^{-3}$
20-30%	-0.006002 x + 0.9168	$4.17 \cdot 10^{-3}$	-0.01089 x + 0.8679	$4.34 \cdot 10^{-3}$
10-20%	-0.01818 x + 0.8456	$3.01 \cdot 10^{-3}$	-0.007458 x + 0.7838	$3.70 \cdot 10^{-3}$
5-10%	0.003776 x + 0.7762	$3.55 \cdot 10^{-3}$	-0.0009687 x + 0.7231	$1.81 \cdot 10^{-3}$
0-5%	-0.003485 x + 0.7538	$2.87 \cdot 10^{-3}$	-0.002785 x + 0.6777	$1.84 \cdot 10^{-3}$

Table 6.5.: Summary of antiproton and antineutron fits in Au–Au collisions at 62.4 GeV for EPOS.

6. Correcting the Event Generator

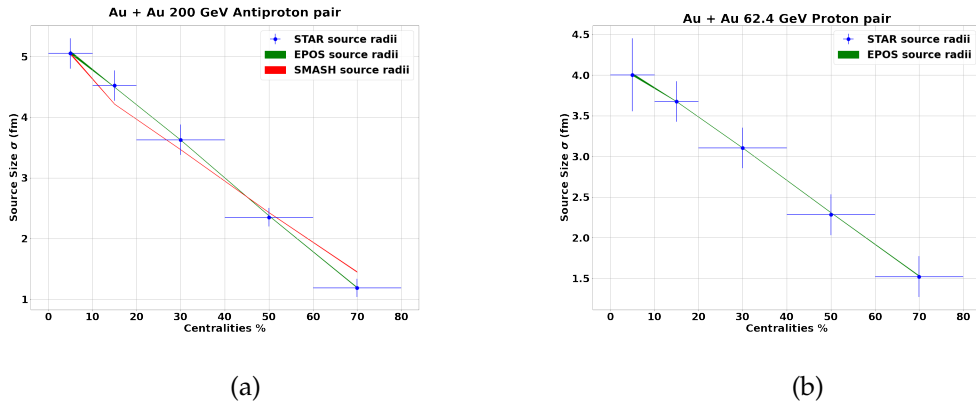


Figure 6.7.: Antiproton pair source radii at 200 GeV for different centrality classes obtained from EPOS (green) and SMASH (red) after correction, compared to STAR Data (blue) (a). Proton pair source radii at 62.4 GeV for different centrality classes obtained from EPOS after correction (green) compared to STAR Data (blue) (b).

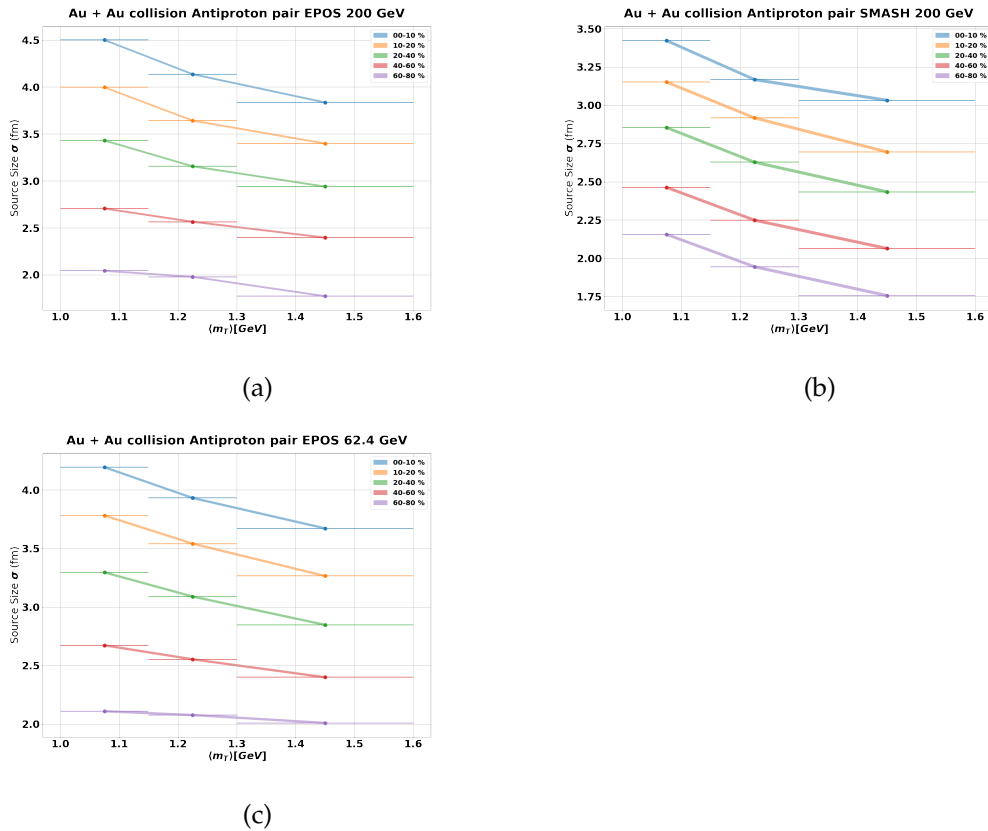


Figure 6.8.: Source size m_T scaling at three different m_T bins and 5 different centralities. EPOS at 200 GeV (a), SMASH at 200 GeV (b), and EPOS at 62.4 GeV (c)

6. Correcting the Event Generator

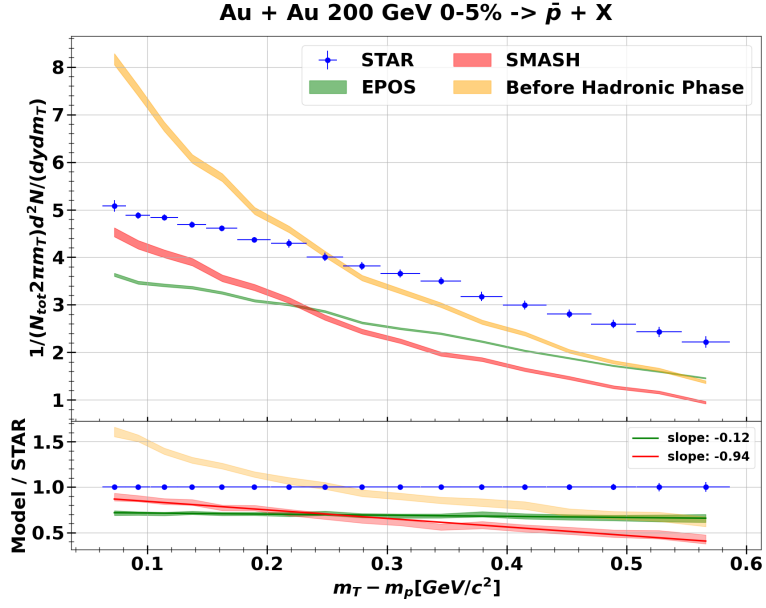


Figure 6.9.: $m_T - m_p$ spectra for antiprotons at 200 GeV for 0-5 % centrality obtained from STAR Data (blue) [66] compared to models from EPOS (green), SMASH (red), and production before the Hadronic phase (orange).

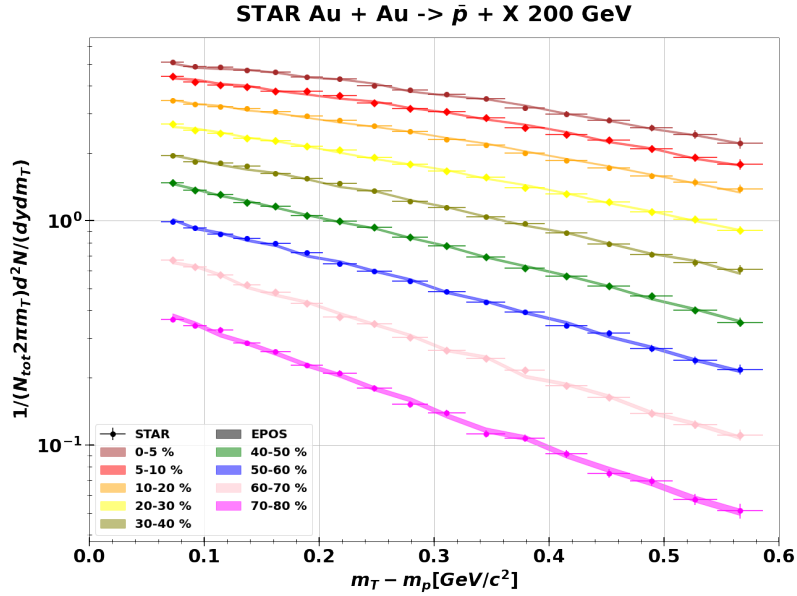


Figure 6.10.: Corrected $m_T - m_p$ spectra for antiprotons at nine different centrality classes from an EPOS production at 200 GeV. Experimental data from STAR taken from [64].

6. Correcting the Event Generator

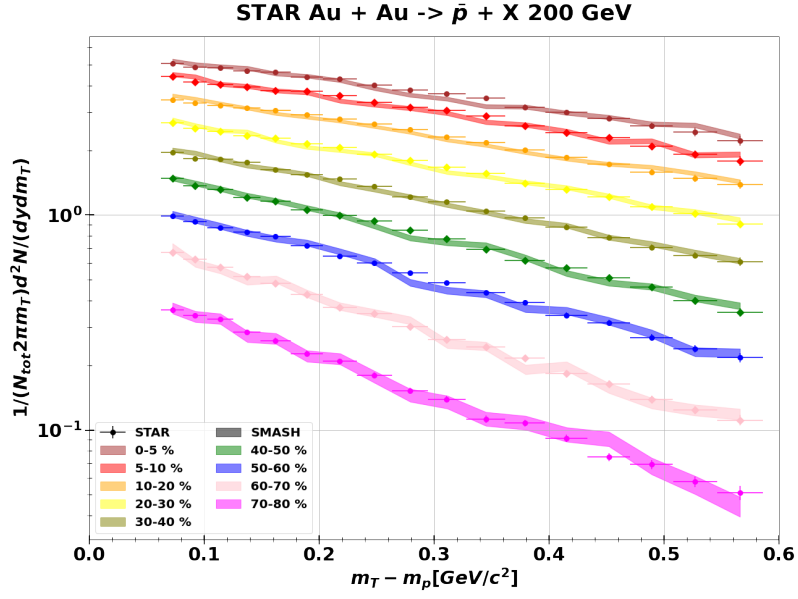


Figure 6.11.: Corrected $m_T - m_p$ spectra for antiprotons at nine different centrality classes from a SMASH production at 200 GeV. Experimental data from STAR taken from [64].

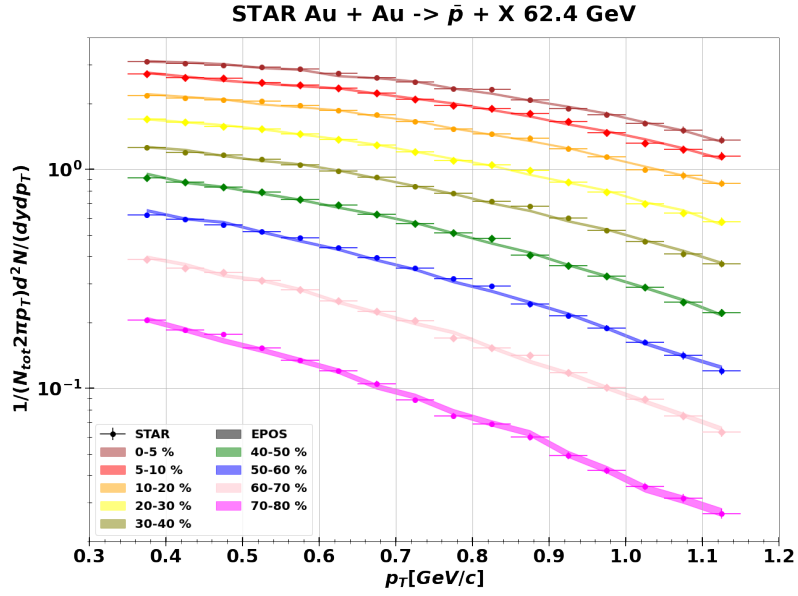


Figure 6.12.: Corrected p_T spectra for antiprotons at nine different centrality classes from an EPOS production at 62.4 GeV. Experimental data from STAR taken from [66].

7. (Anti-)deuteron production spectra

Following the principle of the Wigner function Coalescence Model explained in Sec. 2.2.2 and using the correction scheme developed in Sec. 6.1, the integrated yields for (anti-)deuterons at different centrality classes are presented in this chapter for energies of 200 GeV and 62.4 GeV and compared to experimental data from the STAR Collaboration [67].

In Fig. 7.1, an EPOS production at 200 GeV is compared to experimental data for antideuterons. One can see that the model prediction can reproduce the shape of the experimental data. In the upper panel, the antideuteron yields for central (0-10 %), mid-central (20-40 %), and peripheral events (60-80 %) predicted by EPOS are exemplarily presented. The lower panel shows all five centralities' models and STAR data ratios. EPOS predictions for most central and mid-central events (0-60 %) reproduce the data from STAR with a factor of ~ 1.5 -2.5 for most p_T bins. EPOS's best predictions at 200 GeV lie within the mid-central (10-40 %) events. Finally, for peripheral (60-80 %) events, EPOS fails to reproduce the data with a difference in the ratio of a factor of ~ 2.5 -3.5 for most p_T bins.

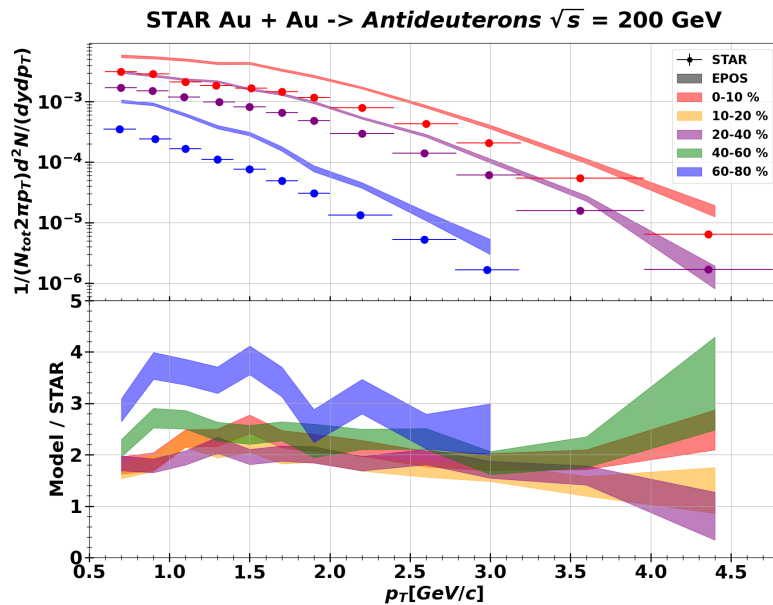


Figure 7.1.: Comparison of EPOS corrected antideuteron integrated yields at 200 GeV for five different centrality classes with STAR Collaboration. Data taken from [67].

In Fig. 7.2, an EPOS production at 200 GeV is compared to experimental data for

7. (Anti-)deuteron production spectra

deuterons. The model predictions can reproduce the shape of the experimental data. In the upper panel, the deuteron yields for central (0-10 %), mid-central (20-40 %), and peripheral events (60-80 %) predicted by EPOS are exemplarily presented. The lower panel shows all five centralities' models and STAR data ratios. EPOS predictions for most central and mid-central events (0-60 %) reproduce the data from STAR with a factor of ~ 1.0 - 2.0 for most p_T bins. EPOS's predictions for deuterons at 200 GeV work consistently within uncertainties. For peripheral (60-80 %) events, EPOS fails to reproduce the data with a difference in the ratio of a factor of ~ 2.0 - 3.0 for most p_T bins.

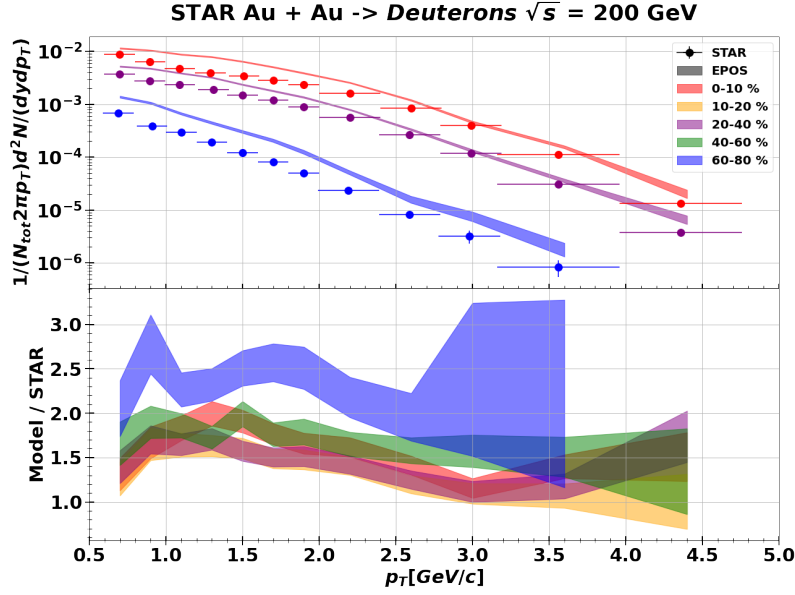


Figure 7.2.: Comparison of EPOS corrected deuteron integrated yields at 200 GeV for five different centrality classes with STAR Collaboration. Data taken from [67].

In Fig. 7.3, the EPOS+SMASH prediction for 200 GeV is compared to experimental antideuteron data. In the upper panel, the antideuteron yields for central (0-10 %), mid-central (20-40 %), and peripheral events (60-80 %) predicted by SMASH are presented. In this case, the model cannot reproduce the shape of the data. The model predictions are similar for most central and mid-central events (0-60 %), finding the worst performance for most peripheral events (60-80 %). The lower panel shows all five centralities' models and STAR data ratios. SMASH predictions for most central events and mid-central (0-60 %) events reproduce the data from STAR with a factor of ~ 4 for lower p_T bins and show a factor of ~ 2 for the mid and higher p_T bins, lying with a factor of ~ 1.5 with errors. For peripheral (40-60 %) events, SMASH reproduces the data similar to mid-central events with the difference that for high p_T bins, the model does not reproduce the experimental data and differs with a factor up to 4. Finally, for peripheral (60-80 %) events SMASH fails to reproduce the data with a difference in the ratio of ~ 5 for lower p_T bins and ~ 7 for higher p_T bins.

7. (Anti-)deuteron production spectra

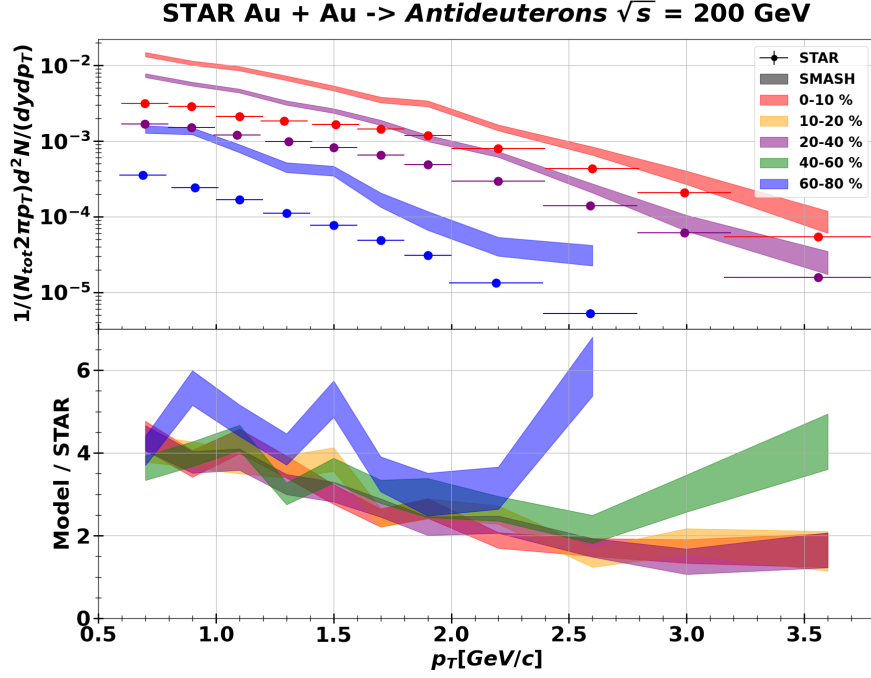


Figure 7.3.: Comparison of SMASH corrected antideuteron integrated yields at 200 GeV for five different centrality classes with STAR Collaboration. Data taken from [67].

In Fig. 7.4, the EPOS+SMASH prediction for 200 GeV is compared to experimental deuteron data. In the upper panel, the deuteron yields for central (0-10 %), mid-central (20-40 %), and peripheral events (60-80 %) predicted by SMASH are presented. The model cannot reproduce the shape of the data for lower p_T bins. The lower panel shows all five centralities' models and STAR data ratios. SMASH predictions for most central events and mid-central (0-60 %) events reproduce the data from STAR with a factor of ~ 3 for lower p_T bins and show a factor of $\sim 1-2$ for the mid and higher p_T bins, lying with a factor of ~ 1.5 with errors. For peripheral (60-80 %) events, SMASH fails to reproduce the data with a difference in the ratio of ~ 3.5 for lower p_T bins and ~ 4 for higher p_T bins.

After presenting both antideuteron productions from EPOS and SMASH at 200 GeV, a ratio between the two models is presented in Fig. 7.5 at five different centralities, one can see that SMASH overestimates the production of antideuterons with a factor of $\sim 0.5-0.6$ for lower p_T bins. For mid and higher p_T bins, both models are similar in ratio and lie within a factor of $\sim 0.8-1.2$.

In Fig. 7.6, an EPOS production at 62.4 GeV is compared to experimental data. In the upper panel, the antideuteron yields for central (0-10 %), mid-central (20-40 %), and peripheral events (60-80 %) predicted by EPOS are presented. The model prediction can reproduce the shape of the experimental data. The lower panel shows the ratio between the model and the STAR data for five centralities. EPOS predictions for most

7. (Anti-)deuteron production spectra

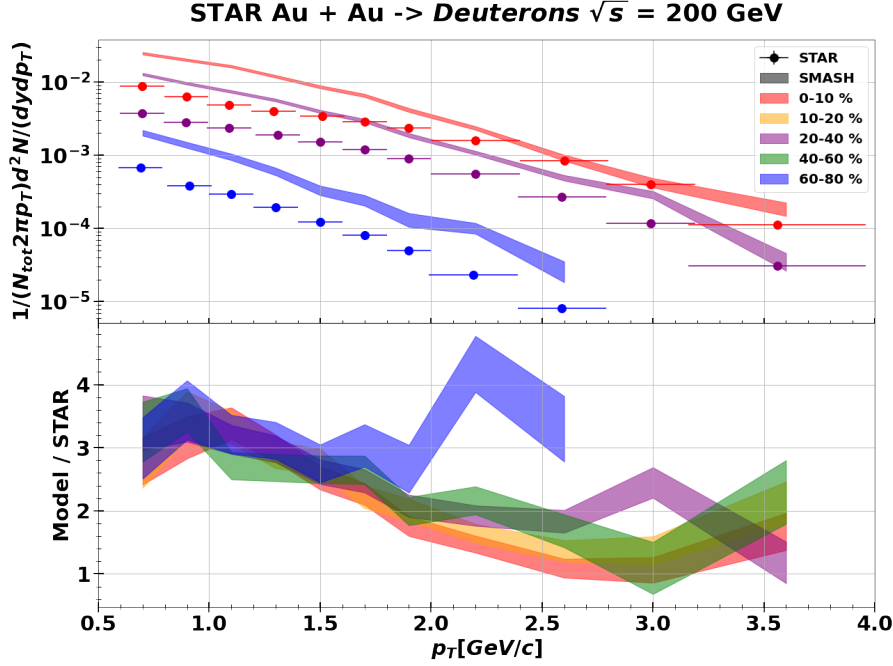


Figure 7.4.: Comparison of SMASH corrected deuteron integrated yields at 200 GeV for five different centrality classes with STAR Collaboration. Data taken from [67].

central events (0-10 %) fail to reproduce the data from STAR with a factor of $\sim 3-4$. EPOS predictions for mid-central and peripheral events (10-80%) reproduce the data from STAR with a factor of $\sim 1.5-3$.

In Fig. 7.7, an EPOS production at 62.4 GeV is compared to experimental data. In the upper panel, the deuteron yields for central (0-10 %), mid-central (20-40 %), and peripheral events (60-80 %) predicted by EPOS are presented. The lower panel shows the ratio between the model and the STAR data for five centralities. EPOS predictions for most central and mid-central events (0-40 %) fail to reproduce the data from STAR with a factor of $\sim 1.5-3$ for lower p_T bins. They can reproduce the data's shape and values within uncertainties for higher p_T bins. EPOS predictions for mid-central and peripheral events (40-80%) can reproduce the data from STAR with a factor of $\sim 0.8-1.5$ for most p_T bins.

After presenting the three different predictions for (anti-)deuteron spectra, it is shown that the SMASH prediction cannot reproduce the shape of the data and fails to predict the yields for antideuterons and deuterons. For EPOS prediction at 200 GeV, the Event generator can consistently reproduce the shape of the spectra for (anti-)deuterons but fails at the yield around factor ~ 2 for most centralities. EPOS prediction at 62.4 GeV reproduces the shape of the data for antideuterons but fails to model the shape for deuterons. The best performances for antideuterons lie for most central events at 200 GeV and for most peripheral events at 62.4 GeV.

7. (Anti-)deuteron production spectra

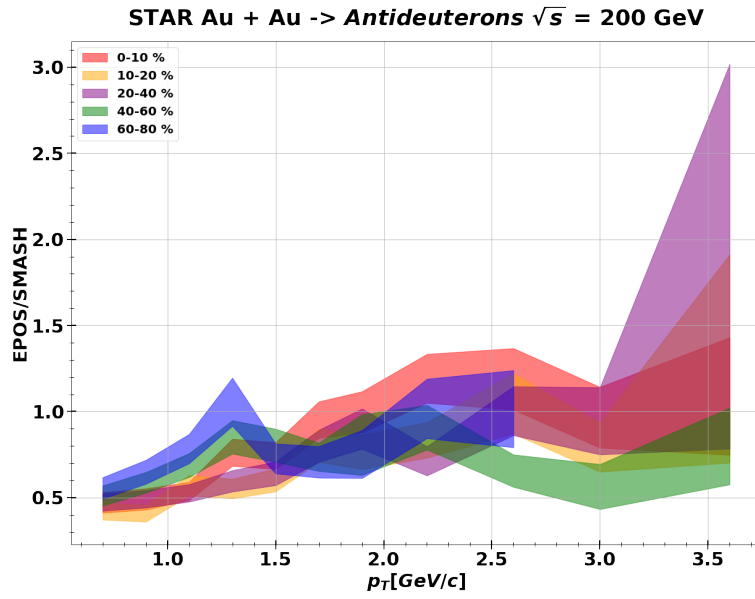


Figure 7.5.: Comparison of EPOS corrected antideuteron integrated yields at 200 GeV for five different centrality classes with SMASH corrected antideuteron integrated yields.

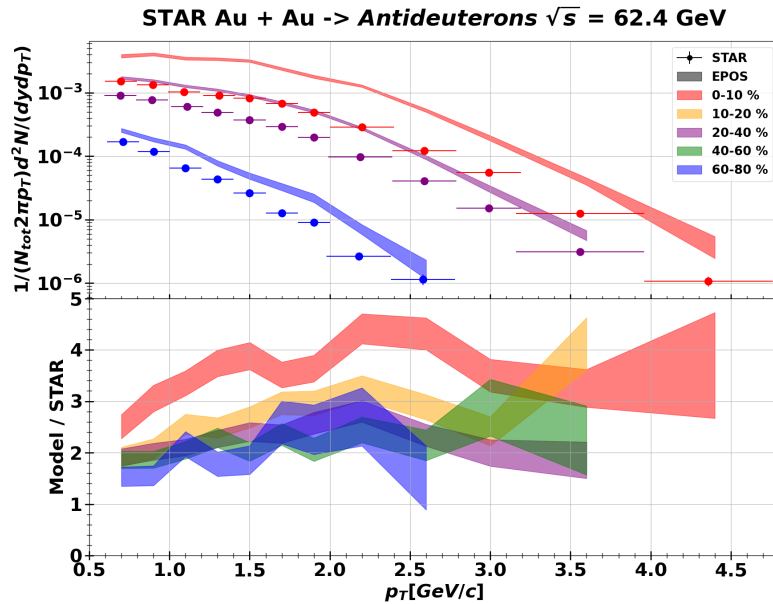


Figure 7.6.: Comparison of EPOS corrected antideuteron integrated yields at 62.4 GeV for five different centrality classes with STAR Collaboration. Data taken from [67].

7. (Anti-)deuteron production spectra

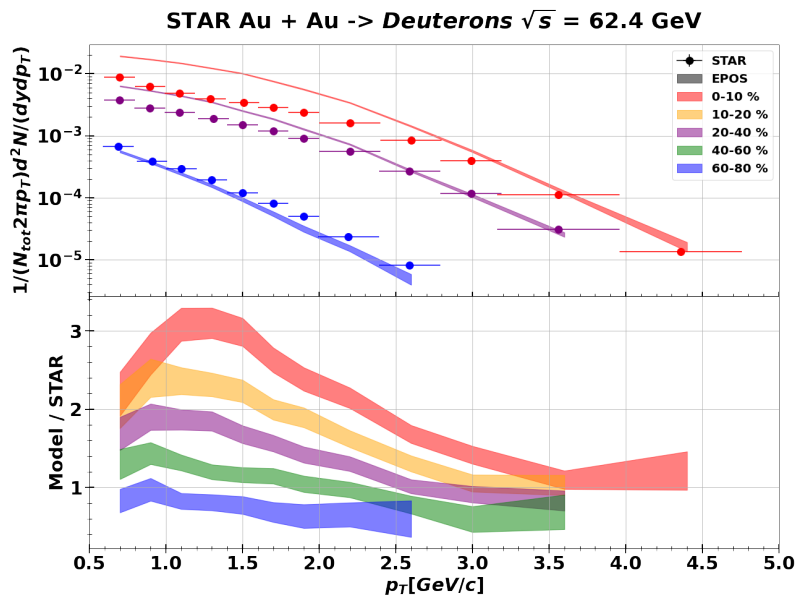


Figure 7.7.: Comparison of EPOS corrected deuteron integrated yields at 62.4 GeV for five different centrality classes with STAR Collaboration Data taken from [67].

8. Summary and Outlook

This work describes and investigates the Wigner function coalescence model as the mechanism for light nuclei formation. The most simple form of coalescence, the spherical approximation, is described and complemented with an advanced implementation based on the Wigner Function of the deuteron, a recent model in coalescence studies. EPOS3 is employed to make (anti-)deuteron predictions using the coalescence model on an event-by-event basis. Further, the rescattering, implemented in EPOS as HACAS, has also been tested using the standalone model SMASH as an afterburner to the EPOS results without HACAS. A correction for the event generators EPOS and SMASH is presented for correctly determining multiplicity classes, known as centrality, source size measurements, and momentum distributions. This correction is then used to predict antideuteron yields using a coalescence afterburner for Au–Au collisions at 200 GeV and 62.4 GeV, compared to experimental data from the STAR collaboration.

The predictions obtained from the EPOS event generator can reproduce the shape of the experimental data. The disparity between the model and the experimental data lies within a factor of ~ 2 for most central and mid-central events in the complete p_T range at both 200 GeV and 62.4 GeV energies. For peripheral events, EPOS cannot reproduce the data for the production at 200 GeV but succeeds in predicting the antideuteron yields at 62.4 GeV. The SMASH transport model cannot explain the shape of the data at a lower p_T range with a disparity in the yields from antideuterons of a factor ~ 4 . For the higher p_T bins, the SMASH transport model can reproduce the shape of the data for all centralities within a factor ~ 2 between the model and the STAR data.

Au–Au collisions give access to heavy-ion collisions at different energies and centralities and allow the study of two-body light nuclei (antinuclei) within the scope of coalescence as a first stage to understand future three-body experiments. Future studies will include a test for the Wigner Function Coalescence Model at a wide range of collision energies to address the model's validity and access the lower part of the p_T region. Further, a study on the difference between EPOS late-stage production and the SMASH transport model needs to be performed to understand the slight difference in the UrQMD model used by these two due to the difference in shape for the antideuteron yields. With the coalescence model presented, a possibility for modeling the formation of (anti)deuterons without any free parameters is implemented. Thus making the model appealing to study different productions for heavy-ion collisions at different energies.

A. Appendix - SMASH Afterburner

A.1. Configuration file

To initialize the SMASH transport model, a configuration file in .txt format is needed. This configuration file includes information about the method used, the external files needed, and other characteristics used in the simulation. An example of a configuration file used in SMASH is shown in Fig. A.1.

- *Logging* refers to the information displayed to help the user follow the simulation. In this case, the complete information is shown using *INFO*.
- *General* is needed to choose between the different modes of initialization and give information about the simulation performed. The mode *List* is chosen, where an input list of particles is used as an afterburner. An example is shown in Sec. A.2. *TimeStepMode* is chosen to be Fixed in time steps of 0.1 fm, specified by *Deltatime*. The *EndTime*, expressed in fm, is explained as how much further the particles in the simulation will be propagated. *Randomseed* gives the possibility to the user to choose between different seeds for the simulation. Finally, *Nevents* specifies the total number of events the simulation will carry.
- *Output* gives information about how the output file for the simulation is obtained. *Outputinterval* is explained as the interval expressed in fm, in which information about the simulation will be printed to help the user. *Particles* refers to the output particles obtained by SMASH after the simulation. *Format* is the output format in which the output file is written. *Onlyfinal* gives the possibility to the user to obtain just final particles after the hadronic rescattering and resonance decays or all the particles created in between these processes.
- *Modi* specifies the method used by SMASH, in this case being an input *List* of predefined particles. *Filedirectory* gives the location of the file used. *Fileprefix* is the name of the file used. Finally, *ShiftId* gives the possibility to use many files, if the split of a big input file is needed.

A.2. Input List of Particles

In Fig. A.2, a representation of the input list of particles in .txt format is shown. This list follows the same format as the SMASH production used in this work. The Header of the file specifies the format in which the subsequent lines are explained. Each line represents a particle. In this sense, the first four values will be for the 4 – *position*

A. Appendix - SMASH Afterburner

```

Logging:
  default: INFO

General:
  Modus:      List
  Time_Step_Mode: Fixed
  Delta_Time: 0.1
  End_Time:   10.0
  Randomseed: -1
  Nevents:    498999

Output:
  Output_Interval: 5.0
  Particles:
    Format:      ["Root"]
    Only_Final:  Yes

Modi:
  List:
    File_Directory: "particle_lists_in"
    File_Prefix: "multiplicity_200gev_20210125_smash_input"
    Shift_Id: 1

```

Figure A.1.: Example of a configuration file used by SMASH transport model to initialize a simulation.

```

#IOSCAR2013 particle_lists t x y z mass p0 px py pz pdg ID charge
# Units: fm fm fm fm GeV GeV GeV GeV GeV none none none
# event 0
3.44141 -1.95891 1.65509 2.66571 0.134977 0.178225 -0.029745 -0.0782639 -0.0808701 111 57 0
3.44141 -1.88774 1.49366 2.66571 0.13957 0.158175 -0.033807 -0.0638938 0.0177226 -211 57 -1
3.44141 -0.689852 1.88756 2.66571 0.938272 1.33337 -0.0616636 -0.137963 0.935243 2212 57 1
3.35838 0.806455 -0.349676 -0.991853 0.13957 0.386479 0.26886 -0.213235 -0.110136 211 57 1
1.71076 -2.20376 0.64391 -0.528001 0.13957 0.187444 -0.0614571 -0.0947023 -0.0539492 -211 57 -1
0.248215 -1.06485 2.59993 -0.079476 0.13957 0.190557 -0.0897583 -0.0847173 -0.0399806 211 57 1
...
# event 0 end
# event 1
3.51288 -1.95891 1.65509 2.66571 0.134977 0.178158 -0.029745 -0.0782639 -0.080722 111 59 0
3.51288 -1.88774 1.49366 2.66571 0.13957 0.158171 -0.033807 -0.0638938 0.0176901 -211 59 -1
3.51288 -0.689852 1.88756 2.66571 0.938272 1.33217 -0.0616636 -0.137963 0.933531 2212 59 1
0.190293 0.315564 2.36434 0.12021 0.13957 0.521687 -0.27501 0.324858 0.267423 211 59 1
0.684839 -1.64 1.70776 0.521669 0.939565 1.43265 -0.0657834 0.285002 1.04123 2112 59 0
0.962862 -0.51761 2.2417 0.428133 0.493677 0.776908 0.293612 -0.401611 0.335226 -321 59 -1
...
# event 1 end
# event 2
3.47808 -1.95891 1.65509 2.66571 0.134977 0.178129 -0.029745 -0.0782639 -0.0806586 111 54 0
...

```

Figure A.2.: Representation of the input list of particles for the initialization of the SMASH Afterburner simulation.

of the particle in fm, following a value for the mass in GeV, then four values for the 4 – *momentum* of the particle in GeV, a code to differentiate between types of particles in PDG convention, an ID and finally the charge of the particle. Each group of particles is separated between events, starting from event 0 and also specifying when the event ends.

Acknowledgments

I want to express my heartfelt gratitude to my thesis supervisors, Professor Dr. Laura Fabbietti and Maximilian Horst, for their unwavering guidance, encouragement, and support throughout the research process. Their expertise and insights have been invaluable, shaping the direction of this study and contributing significantly to its quality.

I am deeply thankful to the Dense and Strange Hadronic Matter of the Physics Department at TUM for providing a stimulating academic environment. I appreciate the discussions, debates, and seminars that have broadened my understanding of physics and inspired me to delve deeper into my research.

Special thanks to my friends for their constant encouragement and understanding. Their unwavering support has been my strength, enabling me to overcome challenges and focus on my goals.

I am deeply grateful to my family, parents, and sister for their unconditional love, patience, and support. Your belief in my potential has been my guiding light, and I am fortunate to have you by my side.

This thesis would not have been possible without the collective support and encouragement of all these individuals and organizations. Thank you for believing in me and being part of this important milestone in my academic journey.

List of Figures

1.1. Graphical representation of the antideuteron production channels present in our Universe and measured on Earth. Primary contributions are carried by two matter particles annihilating into a W^+W^- pair, decaying into an antideuteron and other products. Secondary production occurs when high-energy cosmic rays collide with atoms from the interstellar medium. Tertiary channels include antideuterons that scatter off the interstellar medium, elastically losing momentum compared to secondary antideuterons.	2
2.1. Space-time diagram illustrating the evolution of a central heavy ion collision. The z -axis represents the direction parallel to the beam line. The diagram highlights two scenarios: on the right, the presence of a QGP, while on the left, the absence of it. Taken from [16]	5
2.2. Three different statistical hadronization model fits the selected mesons, hadrons, and light (anti-)nuclei yields in Pb-Pb collisions at $\sqrt{s_{NN}}=2.76$ TeV. Taken from [20].	6
2.3. Graphical representation of a proton-neutron pair, where a proton is within a sphere of radius p_0 in momentum-space around a neutron. . .	8
2.4. Deuteron wave functions using different potential configurations, Gaussian (red), Hulthén (green) [32], χ EFT N ⁴ LO S-wave and D-wave (orange) [33] and Argonne v18 S-wave and D-wave (blue) [34]. Taken from [31] .	11
2.5. Impact parameter b and a graphical representation of the colliding nuclei in the transverse plane. Z axis represents the beam direction while X and Y the reaction plane. The blue lines represent the lab axis with Ψ_{RP} the reaction plane angle. Adapted from [35].	12
3.1. Elementary parton-parton scattering (a). Multiple interactions between parton ladders in parallel. x_{PE} represents the fraction of total momentum for each ladder (b). Taken from [39].	13
3.2. String fragmentation mechanism between two $d\bar{d}$ forming out hadrons at each fragmentation point. Taken from [15].	14
3.3. Schematic representation of the workflow in EPOS. Adapted from [15].	17
4.1. Graphical representation in two dimensions of the cell structure to find actions between particles. Adapted from [44].	21
4.2. Position of nuclei at time of initialization. The Lorentz contracted spheres will touch at $t = 0$ in a central collision. Taken from [44].	22

List of Figures

5.1.	The QCD phase diagram with RHIC energies performed during the BES program and LHC energy at 2.76 TeV is shown in purple. Two energies at 200 GeV and 130 GeV from RHIC are shown in green and blue, respectively. The energies from the first phase of BES are shown in grey (62.4 GeV - 27 GeV). The second phase of the BES is presented in yellow for energies between 19.6 GeV and 7.7 GeV. Finally, the energies performed during the fixed target experiment are shown in red from 7.7 GeV to 3.0 GeV. The presented energies allowed to scan μ_B from 400 MeV to 20 MeV. At the top energies, the QCD calculations predict a cross-over transition with $T \approx 150 - 170$ MeV and $\mu_B \approx 0$ GeV. The first-order transition is present for lower T and higher μ_B for the right side energies. The red line represents the phase transition with its endpoint, the QCD critical point shown in a red circle. Taken from [51].	26
5.2.	Perspective view of the layout of the STAR Experiment. A cutaway is present to see the inner detector systems. Taken from [58].	27
6.1.	Charged particle distributions obtained with EPOS at 200 GeV (green) and 62.4 GeV (blue). The green and blue bands represent the 5% most central events for the multiplicity distributions at 200 GeV and 62.4 GeV, respectively. Both distributions for the multiplicity rapidity density are obtained with a rapidity slice of $ y < 0.1$, similar to the STAR data. . . .	30
6.2.	Comparison of the mean multiplicity rapidity density, $\langle N_{ch}/dy \rangle$, at 200 GeV for STAR data (blue), EPOS (green), and SMASH (red).	31
6.3.	Comparison of the mean multiplicity rapidity density, $\langle N_{ch}/dy \rangle$, at 62.4 GeV for STAR data (blue) and EPOS (green).	32
6.4.	Distance distributions at 0-10 % centrality normalized to the total number of events for antiproton pairs at 200 GeV obtained from EPOS (blue) and SMASH (red). The green points represent the distance between proton pairs at 62.4 GeV for a 0-10 % centrality. The curves are fit using Eq. 6.2 assuming a Gaussian Source.	33
6.5.	Antiproton pair source radii at 200 GeV for different centrality classes obtained from EPOS (green) and SMASH (red) compared to STAR Data (blue) (a). Source radii from STAR (red) against $(dN_{ch}/d\eta)^{1/3}$. An interpolation is performed along the dashed orange line, with the new source radii (orange) at 5 different centralities (b).	34
6.6.	Proton pair source radii at 62.4 GeV for different centrality classes obtained from EPOS (green) compared to STAR Data (blue) (a). Source radii from STAR (red) against $(dN_{ch}/d\eta)^{1/3}$. An interpolation is performed along the dashed orange line, with the new source radii (orange) at 5 different centralities (b).	35
6.7.	Antiproton pair source radii at 200 GeV for different centrality classes obtained from EPOS (green) and SMASH (red) after correction, compared to STAR Data (blue) (a). Proton pair source radii at 62.4 GeV for different centrality classes obtained from EPOS after correction (green) compared to STAR Data (blue) (b).	37

List of Figures

6.8.	Source size m_T scaling at three different m_T bins and 5 different centralities. EPOS at 200 GeV (a), SMASH at 200 GeV (b), and EPOS at 62.4 GeV (c)	37
6.9.	$m_T - m_p$ spectra for antiprotons at 200 GeV for 0-5 % centrality obtained from STAR Data (blue) [66] compared to models from EPOS (green), SMASH (red), and production before the Hadronic phase (orange). . . .	38
6.10.	Corrected $m_T - m_p$ spectra for antiprotons at nine different centrality classes from an EPOS production at 200 GeV. Experimental data from STAR taken from [64].	38
6.11.	Corrected $m_T - m_p$ spectra for antiprotons at nine different centrality classes from a SMASH production at 200 GeV. Experimental data from STAR taken from [64].	39
6.12.	Corrected p_T spectra for antiprotons at nine different centrality classes from an EPOS production at 62.4 GeV. Experimental data from STAR taken from [66].	39
7.1.	Comparison of EPOS corrected antideuteron integrated yields at 200 GeV for five different centrality classes with STAR Collaboration. Data taken from [67].	40
7.2.	Comparison of EPOS corrected deuteron integrated yields at 200 GeV for five different centrality classes with STAR Collaboration. Data taken from [67].	41
7.3.	Comparison of SMASH corrected antideuteron integrated yields at 200 GeV for five different centrality classes with STAR Collaboration. Data taken from [67].	42
7.4.	Comparison of SMASH corrected deuteron integrated yields at 200 GeV for five different centrality classes with STAR Collaboration. Data taken from [67].	43
7.5.	Comparison of EPOS corrected antideuteron integrated yields at 200 GeV for five different centrality classes with SMASH corrected antideuteron integrated yields.	44
7.6.	Comparison of EPOS corrected antideuteron integrated yields at 62.4 GeV for five different centrality classes with STAR Collaboration. Data taken from [67].	44
7.7.	Comparison of EPOS corrected adeuteron integrated yields at 62.4 GeV for five different centrality classes with STAR Collaboration Data taken from [67].	45
A.1.	Example of a configuration file used by SMASH transport model to initialize a simulation.	48
A.2.	Representation of the input list of particles for the initialization of the SMASH Afterburner simulation.	48

List of Tables

3.1. Variables used in EPOS. Multiple purposes can be accessed for different variables and IDs. Adapted from [15].	15
6.1. Summary of centralities in Au–Au collisions at 200 GeV and 62.4 GeV regarding mean multiplicity rapidity density in the rapidity region of $ y < 0.1$. The total errors are obtained from summing statistical and systematic uncertainties in quadrature. Adapted from [64].	29
6.2. Summary of source sizes (in fm) in Au–Au collisions at 200 GeV and 62.4 GeV regarding antiproton-antiproton and proton-proton correlations. The total errors are formed of statistical uncertainties. Adapted from [65].	31
6.3. Summary of antiproton and antineutron fits in Au–Au collisions at 200 GeV for EPOS.	36
6.4. Summary of antiproton and antineutron fits in Au–Au collisions at 200 GeV for SMASH.	36
6.5. Summary of antiproton and antineutron fits in Au–Au collisions at 62.4 GeV for EPOS.	36

Bibliography

- [1] S. Acharya et al. “Measurement of anti-³He nuclei absorption in matter and impact on their propagation in the Galaxy”. In: *Nature Phys.* 19.1 (2023), pp. 61–71. DOI: 10.1038/s41567-022-01804-8. arXiv: 2202.01549 [nucl-ex].
- [2] “Measurement of interaction between antiprotons”. In: *Nature* 527.7578 (Nov. 2015), pp. 345–348. DOI: 10.1038/nature15724. URL: <https://doi.org/10.1038/nature15724>.
- [3] A. Ibarra and S. Wild. “Prospects of antideuteron detection from dark matter annihilations or decays at AMS-02 and GAPS”. In: *Journal of Cosmology and Astroparticle Physics* 2013.02 (Feb. 2013), pp. 021–021. DOI: 10.1088/1475-7516/2013/02/021. URL: <https://doi.org/10.1088/1475-7516/2013/02/021>.
- [4] V. Poulin, P. Salati, I. Cholis, M. Kamionkowski, and J. Silk. “Where do the iAMS-02/i antihelium events come from?” In: *Physical Review D* 99.2 (Jan. 2019). DOI: 10.1103/physrevd.99.023016. URL: <https://doi.org/10.1103/physrevd.99.023016>.
- [5] F. Zwicky. “Die Rotverschiebung von extragalaktischen Nebeln”. In: *Helvetica Physica Acta* 6 (Jan. 1933), pp. 110–127.
- [6] D. H. Rogstad and G. S. Shostak. “Gross Properties of Five Scd Galaxies as Determined from 21-CENTIMETER Observations”. In: 176 (Sept. 1972), p. 315. DOI: 10.1086/151636.
- [7] A. Bosma. “The distribution and kinematics of neutral hydrogen in spiral galaxies of various morphological types”. PhD thesis. University of Groningen, Netherlands, Mar. 1978.
- [8] V. C. Rubin, J. Ford W. K., and N. Thonnard. “Extended rotation curves of high-luminosity spiral galaxies. IV. Systematic dynamical properties, Sa -> Sc.” In: 225 (Nov. 1978), pp. L107–L111. DOI: 10.1086/182804.
- [9] J. Silk et al. *Particle Dark Matter: Observations, Models and Searches*. Ed. by G. Bertone. Cambridge: Cambridge Univ. Press, 2010. ISBN: 978-1-107-65392-4. DOI: 10.1017/CB09780511770739.
- [10] J. R. Bond and G. Efstathiou. “Cosmic background radiation anisotropies in universes dominated by nonbaryonic dark matter”. In: 285 (Oct. 1984), pp. L45–L48. DOI: 10.1086/184362.
- [11] M. Persic, P. Salucci, and F. Stel. “The universal rotation curve of spiral galaxies — I. The dark matter connection”. In: 281.1 (July 1996), pp. 27–47. DOI: 10.1093/mnras/278.1.27. arXiv: astro-ph/9506004 [astro-ph].

Bibliography

- [12] D. Clowe, M. Bradač, A. H. Gonzalez, M. Markevitch, S. W. Randall, C. Jones, and D. Zaritsky. “A Direct Empirical Proof of the Existence of Dark Matter”. In: 648.2 (Sept. 2006), pp. L109–L113. doi: 10.1086/508162. arXiv: astro-ph/0608407 [astro-ph].
- [13] C. A. J. O’Hare, D. Loomba, K. Altenmüller, et al. *Recoil imaging for directional detection of dark matter, neutrinos, and physics beyond the Standard Model*. 2022. arXiv: 2203.05914 [physics.ins-det].
- [14] U. W. Heinz. *Concepts of Heavy-Ion Physics*. 2004. arXiv: hep-ph/0407360 [hep-ph].
- [15] M. Horst. “Study of an antideuteron production mechanism and propagation through the interstellar medium”. In: (2021).
- [16] L. Barioglio. “Study of the production of (anti-) deuterons in pp collisions at the LHC with the ALICE experiment”. PhD thesis. Technische Universitaet Muenchen (DE).
- [17] F. Becattini. *An introduction to the Statistical Hadronization Model*. 2009. arXiv: 0901.3643 [hep-ph].
- [18] E. Fermi. “High-energy nuclear events”. In: *Prog. Theor. Phys.* 5 (1950), pp. 570–583. doi: 10.1143/PTP.5.570.
- [19] S. Mrówczyński. “Production of Light Nuclei in the Thermal and Coalescence Models”. In: *Acta Physica Polonica B* 48 (Apr. 2017), p. 707. doi: 10.5506/APhysPo1B.48.707.
- [20] S. Acharya, D. Adamová, J. Adolfsson, et al. “Production of ^4He and ^3He in Pb–Pb collisions at $\sqrt{s_{\text{NN}}}=2.76\text{TeV}$ at the LHC”. In: *Nuclear Physics A* 971 (Mar. 2018), pp. 1–20. doi: 10.1016/j.nuclphysa.2017.12.004. URL: <https://doi.org/10.1016%2Fj.nuclphysa.2017.12.004>.
- [21] E. Kessler, Jr, M. Dewey, R. Deslattes, A. Henins, H. Börner, M. Jentschel, C. Doll, and H. Lehmann. “The deuteron binding energy and the neutron mass”. In: *Physics Letters A* 255.4 (1999), pp. 221–229. ISSN: 0375-9601. doi: [https://doi.org/10.1016/S0375-9601\(99\)00078-X](https://doi.org/10.1016/S0375-9601(99)00078-X). URL: <https://www.sciencedirect.com/science/article/pii/S037596019900078X>.
- [22] P. Braun-Munzinger, B. Dönigus, and N. Löhner. “ALICE investigates ‘snowballs in hell’”. In: *CERN Courier* 55.7 (2015), pp. 26–30. URL: <https://cds.cern.ch/record/2232490>.
- [23] A. Andronic, P. Braun-Munzinger, J. Stachel, and H. Stöcker. “Production of light nuclei, hypernuclei and their antiparticles in relativistic nuclear collisions”. In: *Physics Letters B* 697.3 (Mar. 2011), pp. 203–207. doi: 10.1016/j.physletb.2011.01.053. URL: <https://doi.org/10.1016%2Fj.physletb.2011.01.053>.
- [24] S. T. Butler and C. A. Pearson. “Deuterons from High-Energy Proton Bombardment of Matter”. In: *Phys. Rev.* 129 (2 Jan. 1963), pp. 836–842. doi: 10.1103/PhysRev.129.836. URL: <https://link.aps.org/doi/10.1103/PhysRev.129.836>.

Bibliography

- [25] M. Kachelrieß, S. Ostapchenko, and J. Tjemsland. “Alternative coalescence model for deuteron, tritium, helium-3 and their antinuclei”. In: *The European Physical Journal A* 56.1 (Jan. 2020). DOI: 10.1140/epja/s10050-019-00007-9. URL: <https://doi.org/10.1140%2Fepja%2Fs10050-019-00007-9>.
- [26] J. I. Kapusta. “Mechanisms for deuteron production in relativistic nuclear collisions”. In: *Phys. Rev. C* 21 (4 Apr. 1980), pp. 1301–1310. DOI: 10.1103/PhysRevC.21.1301. URL: <https://link.aps.org/doi/10.1103/PhysRevC.21.1301>.
- [27] R. Pohl, F. D. Amaro, A. Antognini, F. Biraben, J. M. R. Cardoso, D. S. Covita, A. Dax, S. Dhawan, L. M. P. Fernandes, A. Giesen, T. Graf, T. W. Hänsch, P. Indelicato, L. Julien, C.-Y. Kao, P. Knowles, E.-O. L. Bigot, Y.-W. Liu, J. A. M. Lopes, L. Ludhova, C. M. B. Monteiro, F. Mulhauser, T. Nebel, F. Nez, P. Rabinowitz, J. M. F. dos Santos, L. A. Schaller, K. Schuhmann, C. Schwob, D. Taqqu, J. F. C. A. Veloso, and F. Kottmann. “The size of the proton and the deuteron”. In: *Journal of Physics: Conference Series* 264.1 (Jan. 2011), p. 012008. DOI: 10.1088/1742-6596/264/1/012008. URL: <https://dx.doi.org/10.1088/1742-6596/264/1/012008>.
- [28] A. Ibarra and S. Wild. “Determination of the cosmic antideuteron flux in a Monte Carlo approach”. In: *Phys. Rev. D* 88 (2 July 2013), p. 023014. DOI: 10.1103/PhysRevD.88.023014. URL: <https://link.aps.org/doi/10.1103/PhysRevD.88.023014>.
- [29] R. Scheibl and U. Heinz. “Coalescence and flow in ultrarelativistic heavy ion collisions”. In: *Physical Review C* 59.3 (Mar. 1999), pp. 1585–1602. DOI: 10.1103/physrevc.59.1585. URL: <https://doi.org/10.1103%2Fphysrevc.59.1585>.
- [30] E. Wigner. “On the Quantum Correction For Thermodynamic Equilibrium”. In: *Phys. Rev.* 40 (5 June 1932), pp. 749–759. DOI: 10.1103/PhysRev.40.749. URL: <https://link.aps.org/doi/10.1103/PhysRev.40.749>.
- [31] M. Mahlein, L. Barioglio, F. Bellini, L. Fabbietti, C. Pinto, B. Singh, and S. Tripathy. *Novel parameter-free coalescence model for deuteron production*. 2023. arXiv: 2302.12696 [hep-ex].
- [32] U. Heinz and B. V. Jacak. “Two-Particle Correlations in Relativistic Heavy-Ion Collisions”. In: *Annual Review of Nuclear and Particle Science* 49.1 (Dec. 1999), pp. 529–579. DOI: 10.1146/annurev.nucl.49.1.529. URL: <https://doi.org/10.1146%2Fannurev.nucl.49.1.529>.
- [33] D. R. Entem, R. Machleidt, and Y. Nisyk. “High-quality two-nucleon potentials up to fifth order of the chiral expansion”. In: *Phys. Rev. C* 96 (2 Aug. 2017), p. 024004. DOI: 10.1103/PhysRevC.96.024004. URL: <https://link.aps.org/doi/10.1103/PhysRevC.96.024004>.
- [34] R. B. Wiringa, V. G. J. Stoks, and R. Schiavilla. “Accurate nucleon-nucleon potential with charge-independence breaking”. In: *Phys. Rev. C* 51 (1 Jan. 1995), pp. 38–51. DOI: 10.1103/PhysRevC.51.38. URL: <https://link.aps.org/doi/10.1103/PhysRevC.51.38>.

Bibliography

- [35] D. A. TEANEY. "VISCOUS HYDRODYNAMICS AND THE QUARK GLUON PLASMA". In: *Quark-Gluon Plasma 4*. WORLD SCIENTIFIC, Feb. 2010, pp. 207–266. DOI: 10.1142/9789814293297_0004. URL: https://doi.org/10.1142/2F9789814293297_0004.
- [36] K. Werner. "The hadronic interaction model EPOS". In: *Nuclear Physics B - Proceedings Supplements* 175-176 (2008). Proceedings of the XIV International Symposium on Very High Energy Cosmic Ray Interactions, pp. 81–87. ISSN: 0920-5632. DOI: <https://doi.org/10.1016/j.nuclphysbps.2007.10.012>. URL: <https://www.sciencedirect.com/science/article/pii/S0920563207007736>.
- [37] R. D. Woods and D. S. Saxon. "Diffuse Surface Optical Model for Nucleon-Nuclei Scattering". In: *Phys. Rev.* 95 (2 July 1954), pp. 577–578. DOI: 10.1103/PhysRev.95.577. URL: <https://link.aps.org/doi/10.1103/PhysRev.95.577>.
- [38] T. E. Regge. "Introduction to complex orbital momenta". In: *Il Nuovo Cimento (1955-1965)* 14 (1959), pp. 951–976.
- [39] S. Porteboeuf, T. Pierog, and K. Werner. *Producing Hard Processes Regarding the Complete Event: The EPOS Event Generator*. 2010. arXiv: 1006.2967 [hep-ph].
- [40] K. Werner, F.-M. Liu, and T. Pierog. "Parton ladder splitting and the rapidity dependence of transverse momentum spectra in deuteron-gold collisions at the BNL Relativistic Heavy Ion Collider". In: *Physical Review C* 74.4 (Oct. 2006). DOI: 10.1103/physrevc.74.044902. URL: <https://doi.org/10.1103/physrevc.74.044902>.
- [41] M. Bleicher, E. Zabrodin, C. Spieles, S. A. Bass, C. Ernst, S. Soff, L. Bravina, M. Belkacem, H. Weber, H. Stöcker, and W. Greiner. "Relativistic hadron-hadron collisions in the ultra-relativistic quantum molecular dynamics model". In: *Journal of Physics G: Nuclear and Particle Physics* 25.9 (Sept. 1999), pp. 1859–1896. DOI: 10.1088/0954-3899/25/9/308. URL: <https://doi.org/10.1088/0954-3899/25/9/308>.
- [42] S. Gabriel. "Formation of Quark-Gluon-Plasma: Understanding the energy and system size dependence". PARTICLE ACCELERATORS. PhD thesis. Oct 2018. URL: http://inis.iaea.org/search/search.aspx?orig_q=RN:52006911.
- [43] P. D. Group, P. A. Zyla, R. M. Barnett, et al. "Review of Particle Physics". In: *Progress of Theoretical and Experimental Physics* 2020.8 (Aug. 2020), p. 083C01. ISSN: 2050-3911. DOI: 10.1093/ptep/ptaa104. eprint: <https://academic.oup.com/ptep/article-pdf/2020/8/083C01/34673722/ptaa104.pdf>. URL: <https://doi.org/10.1093/ptep/ptaa104>.
- [44] J. Weil et al. "Particle production and equilibrium properties within a new hadron transport approach for heavy-ion collisions". In: *Phys. Rev. C* 94.5 (2016), p. 054905. DOI: 10.1103/PhysRevC.94.054905. arXiv: 1606.06642 [nucl-th].
- [45] K. Werner, I. Karpenko, T. Pierog, M. Bleicher, and K. Mikhailov. "Event-by-event simulation of the three-dimensional hydrodynamic evolution from flux tube initial conditions in ultrarelativistic heavy ion collisions". In: *Physical Review C* 82.4 (Oct. 2010). DOI: 10.1103/physrevc.82.044904. URL: <https://doi.org/10.1103/physrevc.82.044904>.

Bibliography

- [46] D. Oliinychenko, J. Staudenmaier, V. Steinberg, J. Weil, A. Sciarra, A. Schäfer, H. E. (Petersen), S. Ryu, J. Mohs, G. Inghirami, F. Li, A. Sorensen, D. Mitrovic, L. Pang, H. Roch, void-One, R. Hirayama, O. Garcia-Montero, M. Mayer, N. Kübler, S. Spies, J. Gröbel, and N.-U. Bastian. *smash-transport/smash: SMASH-3.0*. Version SMASH-3.0. Apr. 2023. DOI: 10.5281/zenodo.7870822. URL: <https://doi.org/10.5281/zenodo.7870822>.
- [47] S. Bass. “Microscopic models for ultrarelativistic heavy ion collisions”. In: *Progress in Particle and Nuclear Physics* 41 (1998), pp. 255–369. DOI: 10.1016/S0146-6410(98)00058-1. URL: [https://doi.org/10.1016/S0146-6410\(98\)00058-1](https://doi.org/10.1016/S0146-6410(98)00058-1).
- [48] J. Xu, L.-W. Chen, M. B. Tsang, H. Wolter, Y.-X. Zhang, J. Aichelin, M. Colonna, D. Cozma, P. Danielewicz, Z.-Q. Feng, A. Le Fèvre, T. Gaitanos, C. Hartnack, K. Kim, Y. Kim, C.-M. Ko, B.-A. Li, Q.-F. Li, Z.-X. Li, P. Napolitani, A. Ono, M. Papa, T. Song, J. Su, J.-L. Tian, N. Wang, Y.-J. Wang, J. Weil, W.-J. Xie, F.-S. Zhang, and G.-Q. Zhang. “Understanding transport simulations of heavy-ion collisions at 100A and 400A MeV: Comparison of heavy-ion transport codes under controlled conditions”. In: *Phys. Rev. C* 93 (4 Apr. 2016), p. 044609. DOI: 10.1103/PhysRevC.93.044609. URL: <https://link.aps.org/doi/10.1103/PhysRevC.93.044609>.
- [49] K. Olive. “Review of Particle Physics”. In: *Chinese Physics C* 38.9 (Aug. 2014), p. 090001. DOI: 10.1088/1674-1137/38/9/090001. URL: <https://dx.doi.org/10.1088/1674-1137/38/9/090001>.
- [50] Y. Nara, N. Otuka, A. Ohnishi, K. Niita, and S. Chiba. “Relativistic nuclear collisions at 10A GeV energies from p+Be to Au+Au with the hadronic cascade model”. In: *Physical Review C* 61.2 (Dec. 1999). DOI: 10.1103/physrevc.61.024901. URL: <https://doi.org/10.1103/physrevc.61.024901>.
- [51] G. Odyniec. “Beam Energy Scan Program at RHIC (BES I and BES II) – Probing QCD Phase Diagram with Heavy-Ion Collisions”. In: *PoS CORFU2018* (2019). Ed. by K. Anagnostopoulos et al., p. 151. DOI: 10.22323/1.347.0151.
- [52] J. N. Marx. “The STAR Experiment at RHIC”. In: *Advances in Nuclear Dynamics 2*. Ed. by W. Bauer and G. D. Westfall. Boston, MA: Springer US, 1996, pp. 233–237. ISBN: 978-1-4757-9086-3. DOI: 10.1007/978-1-4757-9086-3_32. URL: https://doi.org/10.1007/978-1-4757-9086-3_32.
- [53] W. J. Marciano and H. Pagels. “Quantum Chromodynamics: A Review”. In: *Phys. Rept.* 36 (1978), p. 137. DOI: 10.1016/0370-1573(78)90208-9.
- [54] M. A. Stephanov. *QCD phase diagram: an overview*. 2006. arXiv: hep-lat/0701002 [hep-lat].
- [55] M. G. Alford, A. Schmitt, K. Rajagopal, and T. Schäfer. “Color superconductivity in dense quark matter”. In: *Rev. Mod. Phys.* 80 (4 Nov. 2008), pp. 1455–1515. DOI: 10.1103/RevModPhys.80.1455. URL: <https://link.aps.org/doi/10.1103/RevModPhys.80.1455>.

Bibliography

- [56] J. Rafelski. “Connecting QGP-Heavy Ion Physics to the Early Universe”. In: *Nuclear Physics B - Proceedings Supplements* 243-244 (2013). Proceedings of the IV International Conference on Particle and Fundamental Physics in Space, pp. 155–162. ISSN: 0920-5632. DOI: <https://doi.org/10.1016/j.nuclphysbps.2013.09.017>. URL: <https://www.sciencedirect.com/science/article/pii/S0920563213005410>.
- [57] A. Bazavov, T. Bhattacharya, C. DeTar, H.-T. Ding, S. Gottlieb, R. Gupta, P. Hegde, U. Heller, F. Karsch, E. Laermann, L. Levkova, S. Mukherjee, P. Petreczky, C. Schmidt, C. Schroeder, R. Soltz, W. Soeldner, R. Sugar, M. Wagner, and P. V. and. “Equation of state in (2+1)-flavor QCD”. In: *Physical Review D* 90.9 (Nov. 2014). DOI: 10.1103/physrevd.90.094503. URL: <https://doi.org/10.1103%2Fphysrevd.90.094503>.
- [58] K. Ackermann, N. Adams, C. Adler, et al. “STAR detector overview”. In: *Nuclear Instruments and Methods in Physics Research Section A: Accelerators, Spectrometers, Detectors and Associated Equipment* 499.2 (2003). The Relativistic Heavy Ion Collider Project: RHIC and its Detectors, pp. 624–632. ISSN: 0168-9002. DOI: [https://doi.org/10.1016/S0168-9002\(02\)01960-5](https://doi.org/10.1016/S0168-9002(02)01960-5). URL: <https://www.sciencedirect.com/science/article/pii/S0168900202019605>.
- [59] M. Anderson, J. Berkovitz, W. Betts, R. Bossingham, F. Bieser, R. Brown, M. Burks, M. C. de la Barca Sánchez, D. Cebra, M. Cherney, J. Chrin, W. Edwards, V. Ghazikhanian, D. Greiner, M. Gilkes, D. Hardtke, G. Harper, E. Hjort, H. Huang, G. Igo, S. Jacobson, D. Keane, S. Klein, G. Koehler, L. Kotchenda, B. Lasiuk, A. Lebedev, J. Lin, M. Lisa, H. Matis, J. Nystrand, S. Panitkin, D. Reichold, F. Retiere, I. Sakrejda, K. Schweda, D. Shuman, R. Snellings, N. Stone, B. Stringfellow, J. Thomas, T. Trainor, S. Trentalange, R. Wells, C. Whitten, H. Wieman, E. Yamamoto, and W. Zhang. “The STAR time projection chamber: a unique tool for studying high multiplicity events at RHIC”. In: *Nuclear Instruments and Methods in Physics Research Section A: Accelerators, Spectrometers, Detectors and Associated Equipment* 499.2-3 (Mar. 2003), pp. 659–678. DOI: 10.1016/S0168-9002(02)01964-2. URL: <https://doi.org/10.1016%2Fs0168-9002%2802%2901964-2>.
- [60] M. Beddo, E. Bielick, T. Fornek, et al. “The STAR Barrel Electromagnetic Calorimeter”. In: *Nuclear Instruments and Methods in Physics Research Section A: Accelerators, Spectrometers, Detectors and Associated Equipment* 499.2 (2003). The Relativistic Heavy Ion Collider Project: RHIC and its Detectors, pp. 725–739. ISSN: 0168-9002. DOI: [https://doi.org/10.1016/S0168-9002\(02\)01970-8](https://doi.org/10.1016/S0168-9002(02)01970-8). URL: <https://www.sciencedirect.com/science/article/pii/S0168900202019708>.
- [61] L. Adamczyk, J. K. Adkins, G. Agakishiev, et al. “Measurement of Longitudinal Spin Asymmetries for Weak Boson Production in Polarized Proton-Proton Collisions at RHIC”. In: *Phys. Rev. Lett.* 113 (7 Aug. 2014), p. 072301. DOI: 10.1103/PhysRevLett.113.072301. URL: <https://link.aps.org/doi/10.1103/PhysRevLett.113.072301>.

Bibliography

- [62] J. Adam et al. “Beam-energy dependence of identified two-particle angular correlations in $\sqrt{s_{NN}} = 7.7\text{--}200$ GeV Au+Au collisions”. In: *Phys. Rev. C* 101.1 (2020), p. 014916. DOI: 10.1103/PhysRevC.101.014916. arXiv: 1906.09204 [nucl-ex].
- [63] L. Šerk šnyt è, S. Königstorfer, P. von Doetinchem, L. Fabbietti, D. M. Gomez-Coral, J. Herms, A. Ibarra, T. Pöschl, A. Shukla, A. Strong, and I. Vorobyev. “Reevaluation of the cosmic antideuteron flux from cosmic-ray interactions and from exotic sources”. In: *Phys. Rev. D* 105 (8 Apr. 2022), p. 083021. DOI: 10.1103/PhysRevD.105.083021. URL: <https://link.aps.org/doi/10.1103/PhysRevD.105.083021>.
- [64] B. I. Abelev, M. M. Aggarwal, Z. Ahammed, et al. “Systematic measurements of identified particle spectra in pp , $d + Au$, and $Au + Au$ collisions at the STAR detector”. In: *Phys. Rev. C* 79 (3 Mar. 2009), p. 034909. DOI: 10.1103/PhysRevC.79.034909. URL: <https://link.aps.org/doi/10.1103/PhysRevC.79.034909>.
- [65] H. P. Gos. “Proton proton, anti-proton anti-proton, proton anti-proton correlations in $Au + Au$ collisions measured by STAR at RHIC”. In: *European Physical Journal C* 49.1 (Jan. 2007), pp. 75–80. DOI: 10.1140/epjc/s10052-006-0099-0.
- [66] J. Adams, C. Adler, M. M. Aggarwal, et al. “Identified Particle Distributions in pp and $Au + Au$ Collisions at $\sqrt{s_{NN}} = 200$ GeV”. In: *Phys. Rev. Lett.* 92 (11 Mar. 2004), p. 112301. DOI: 10.1103/PhysRevLett.92.112301. URL: <https://link.aps.org/doi/10.1103/PhysRevLett.92.112301>.
- [67] J. Adam, L. Adamczyk, J. R. Adams, et al. “Beam energy dependence of (anti-)deuteron production in $Au + Au$ collisions at the BNL Relativistic Heavy Ion Collider”. In: *Phys. Rev. C* 99 (6 June 2019), p. 064905. DOI: 10.1103/PhysRevC.99.064905. URL: <https://link.aps.org/doi/10.1103/PhysRevC.99.064905>.